Article:
Liu, X., Iamvasant, C., Liu, C. et al. (2 more authors) (2016) CrCuAgN PVD nanocomposite coatings: Effects of annealing on coating morphology and nanostructure. Applied Surface Science, 392. pp. 732-746. ISSN 0169-4332

https://doi.org/10.1016/j.apsusc.2016.09.011

CrCuAgN PVD Nanocomposite Coatings: Effects of Annealing on Coating Morphology and Nanostructure

Xingguang Liu, Allan Matthews, Adrian Leyland

Abstract

CrCuAgN PVD nanocomposite coatings were produced using pulsed DC unbalanced magnetron sputtering. This investigation focuses on the effects of post-coat annealing on the surface morphology, phase composition and nanostructure of such coatings. In coatings with nitrogen contents up to 16 at.%, chromium exists as metallic Cr with N in supersaturated solid solution, even after 300 ^{o}C and 500 ^{o}C post-coat annealing. Annealing at 300 ^{o}C did not obviously change the phase composition of both nitrogen-free and nitrogen-containing coatings; however, 500 ^{o}C annealing resulted in significant transformation of the nitrogen-containing coatings. The formation of Ag aggregates relates to the (Cu+Ag)/Cr atomic ratio (threshold around 0.2), whereas the formation of Cu aggregates relates to the (Cu+Ag+N)/Cr atomic ratio (threshold around 0.5). The primary annealing-induced changes were reduced solubility of Cu, Ag and N in Cr, and the composition altering from a mixed ultra-fine nanocrystalline and partly amorphous phase constitution to a coarser, but still largely nanocrystalline structure. It was also found that, with sufficient Cu content (> 12 at.%), annealing at a moderately high temperature (e.g. 500 ^{o}C) leads to transportation of both Cu and Ag (even at relatively low concentrations of Ag, ≤ 3 at.%) from inside the coating to the coating surface, which resulted in significant reductions in friction coefficient, by over 50% compared to that of the substrate (from 0.31 to 0.14 with a hemispherical diamond indenter, and from 0.83 to 0.40 with an alumina ball counterface, respectively). Results indicate that the addition of both Cu and Ag (in appropriate

concentrations) to nitrogen-containing chromium is a viable strategy for the development of ‘self-replenishing’ silver-containing thin film architectures for temperature-dependent solid lubrication requirements or antimicrobial coating applications.

Keywords

Nanocomposite; PVD coatings; Annealing; Transportation; Phase transformation; Nanostructure

1. Introduction

In recent years, self-lubricating PVD tribological thin films have been intensively investigated [1-16]. Among these, PVD nanocomposite coatings containing soft metals (e.g. Ag or Cu), as a solid lubrication phase, embedded in a hard wear-resistant matrix, such as a transition metal nitride [2-4, 6-9], carbide [10, 13] or oxide [14-16], and mixtures of these ceramics (in ternary/quaternary/nanocomposite coating systems), have all been extensively studied, with the promise of improved tribological performance during transient and/or cyclic temperature changes [17-19]. In particular, coatings based on Cr-Ag-N [7, 8, 17-21] and Cr-Cu-N [6, 22, 23] (as two typical coating systems), have been studied. For coatings in the Cr-Ag-N system, it is revealed that Ag precipitates often tend to exhibit a lamellar shape (height/width: ~ 1/2 to 1/3), with a uniform, but isolated distribution in the ceramic nitride matrix of the deposited coating [24, 25]. However, for coatings in the Cr-Cu-N system, it is typically found that a metastable solid solution phase of Cu in bcc Cr (with Cu content of up to 60 at.%) will form at low deposition temperatures [26] (e.g. $\leq$ 200 °C), or that nanocrystalline Cr (or CrN if nitrogen is introduced) embedded in a semi-continuous Cu-rich intergranular 'tissue', will form – as was experimentally verified by a number of studies (e.g. Baker et al. [27], Lee et al. [28]).

The hardness to elastic modulus (H/E) ratio is now widely recognised as being a more important and effective property optimisation parameter than hardness (H) alone in defining the mechanical behaviour of tribological coatings on relatively soft and/or compliant substrates (such as low-alloy steels, light metals and other non-ferrous alloys), especially in applications other than cutting and forming operations [27, 29-32]. However, it is important - particularly for metallic nanostructured and amorphous tribological coatings - that this parameter is considered together with other factors

such as system tribochemistry and oxidation kinetics (depending on the operating environment and choice of counterface material).

In a previous study [33], CrCuAgN coatings with different Cu/Ag concentration ratios were produced reactively by unbalanced magnetron sputtering of a composite target (silver ‘buttons’ embedded in a copper plate) and a pure chromium target at three different nitrogen flow rates (0 sccm, 5 sccm and 10 sccm). The nanostructure, morphology and mechanical properties were systematically studied; moreover, a promising coating with moderately high hardness of 14.1 GPa, H/E ratio of 0.072 and a combined Cu+Ag concentration approaching 15 at.% was identified. In the present work, a selection of such CrCuAgN coatings were annealed at 300 °C and 500 °C, for 2 hours. The chamber was heated under high vacuum from ambient at a heating rate of ~15 °C/min, then held at the prescribed annealing temperature for two hours. After annealing, the chamber was cooled back to room temperature under vacuum. The effects of annealing on the nanostructure, surfaced topography, fracture morphology, elemental distribution (and resulting phase composition and mechanical properties) of these coatings were investigated.

2. Experimental procedure

Three groups of coatings were produced prior to annealing, deposited at nitrogen reactive gas flow rates of 0 sccm (control group), 5 sccm and 10 sccm, respectively. Each group contained 5 samples, which were located at 5 different positions between the Cu-Ag composite target and pure Cr target during deposition, as shown schematically in Fig. 1. The chamber was evacuated to a base pressure of 2×10^{-5} mbar (2×10^{-3} Pa) before deposition process. During deposition, the substrates were biased at a DC pulsed voltage of -100V, with a frequency of 180kHz and substrate current density of ~0.4 mA/cm^2. Cr and Cu-Ag targets were powered at 1000W and 400W, respectively. The detailed deposition process, including pre-deposition preparation, sputter target configuration and deposition pressure/voltage parameters, have been described in detail previously [33].

High-resolution secondary electron images were obtained using a Philips XL30 S field emission gun scanning electron microscope (FEG-SEM), in order to observe the morphologies of coated surfaces and fracture sections.

X-ray diffraction (XRD) measurements were carried out using a Siemens D5000 X-ray diffractometer, with a Cu-Kα source (λ=0.15418 nm) and Bragg-Brentano θ-2θ scanning mode, for phase composition analysis of the deposited coatings. In order to distinguish coating diffraction peaks from those of the substrate, a diffraction pattern for the uncoated AISI 316 L stainless steel coupons was also obtained.

Transmission electron bright field images, and dark field images with corresponding selected-area electron diffraction (SAED) patterns were obtained using Philips EM420 and FEI Tecnai T20 transmission electron microscopes (TEMs), in order to assess the phase transformations caused by annealing. All TEM samples were

prepared using an FEI Quanta 200 3D scanning electron microscope equipped with Focused Ion Beam (FIB), with the foil sample surface being parallel to the coating surface.

In order to evaluate the solid lubricating performance of the as-deposited and annealed CrCuAgN coatings, coefficients of friction (CoF) at room temperature (RT) was obtained using a laboratory scratch adhesion test instrument, equipped with a 0.2mm radius Rockwell C hemispherical diamond indenter. The critical load (L_c) of each selected sample was obtained first. Then, a fixed normal load of 20N (significantly lower than the L_c of all tested coatings) was used to obtain the CoF. A scratch speed of 0.2mm/s and distance of 5mm were used in all tests. Moreover, a Bruker CETR-UMT instrument equipped with a high temperature reciprocating sliding wear test module was used to evaluate the tribological properties at RT, 300 °C and 500 °C. An alumina ball of ¼ inch (6.35 mm) diameter was used as the counterface. Normal load, sliding distance and frequency were 1 N, 1 mm and 1Hz, respectively.

In order to simplify the description and analysis in the following sections, each sample (or the deposited coating thereon) from the positions Px (x=1, 2, 3, 4, 5) will be simply described using "Px" (unless otherwise stated). As-deposited coatings without annealing will be described as Px-AD, and coatings annealed at 300 °C and 500 °C will be described as Px-300 and Px-500, respectively. Each group of samples deposited at 0 sccm, 5 sccm and 10 sccm N_2 flow rates will be briefly described as "control group" (or "0 sccm group"), "5 sccm group" and "10 sccm group", respectively. The as-deposited group, 300 °C and 500 °C annealed groups will likewise be described as "0 sccm-AD", "5 sccm-300", etc. The simplified descriptions may be used as a combination as well, e.g. "5 sccm-P1-300" means "sample deposited

at position 1 under a nitrogen reactive gas flow rate of 5 sccm and subsequently vacuum annealed for 2 hours at 300 °C".

3. Results and discussion

The elemental compositions of the coatings investigated in this study are listed in Table 1 [33].

3.1. Fracture cross-sections

The fracture-section secondary-electron images of the as-deposited and annealed coatings are shown in Fig. 2.

3.1.1. The 0 sccm (nitrogen-free) control group

In the 0 sccm (nitrogen-free) control group, the columnar structures of the as-deposited coatings in P1 and P2 became less obvious after 300 °C annealing and even more so after 500 °C annealing. For P3, little difference (except the emergence of fine 'lumps' on the columnar surfaces) was found from 'AD' to '300' then to '500', probably due to its 'native' coarse columnar structure in as-deposited condition compared to the relatively fine columnar structures of P1-AD and P2-AD. For P4 and P5, the fracture sections became gradually more 'lumpy' and rough from "AD", to "300" and then to "500". The blurred columnar boundaries and emergence of 'lumps' on the columnar surfaces after annealing probably indicate the occurrence of phase transformation and will be discussed further in sections 3.3, 3.4 and 3.5.

3.1.2. The 5 sccm and 10 sccm (nitrogen-containing) groups

In the two nitrogen-containing groups (5 sccm group and 10 sccm group), all coatings showed more lumpy and rough fracture-section structures after annealing - and progressively more so with increasing annealing temperature. According to the previous investigation [33], all as-deposited coatings in 5 sccm and 10 sccm groups were substitutionally super-saturated nitrogen-containing chromium (i.e. Cu and Ag in

Cr(N)) and hence likely to be highly metastable. Therefore, it may be expected that precipitates would form during annealing, which could explain the formation of the 'lumps' in the fracture sections of the annealed coatings (and this will be confirmed in the phase transformation analysis in sections 3.4 and 3.5).

3.2. Surface morphology

Oblique-view secondary-electron images of the coating surface morphologies are shown in Fig. 3.

3.2.1. The 0 sccm (nitrogen-free) control group

For the 0 sccm control group, it can be seen that from “AD” to “300” to “500”, coating surfaces become rougher. Some precipitated particles can be seen from 0 sccm-P5-500, as shown by areas circled in Fig. 3.

3.2.2. The 5 sccm and 10 sccm (nitrogen-containing) groups

In the two nitrogen-containing groups, for P1 and P2, no obvious change in surface roughness can be seen from their as-deposited states to their annealed states, as shown in Fig. 3. Some tiny cracks can be seen in 5 sccm-P1-300, 5 sccm-P2-300 and 10 sccm-P2-300. However, no obvious cracks can be seen from P1-500 and P2-500 in both 5 sccm and 10 sccm groups. The surface roughness of P3 in both nitrogen-containing groups changed slightly after annealing; however, no development of surface aggregates could be observed.

For P4 and P5 in the two nitrogen-containing groups, it can be seen that sphere-like (Cu, Ag)-rich (see section 3.3) aggregates emerged and became larger in size from P4 to P5 (and from 300 °C to 500 °C annealing temperature), as shown by the areas circled in Fig. 3.

3.2.3. Comparison among the three coating groups

It was noticed that, after annealing, the number of aggregates found in the nitrogen-containing coatings was much higher than in the nitrogen-free control group, which is probably because the introduction of nitrogen reduced the solubility of Cu (and Ag) in

Cr, therefore more (Cu, Ag)-rich aggregates would form for the nitrogen-containing coatings after annealing. This is further supported by the fact that more (and larger) aggregates were found in the 10 sccm group than in the 5 sccm group.

For both the nitrogen-free control group and the nitrogen-containing groups, voids and spaces between columns can be clearly seen in the coatings with high Cu+Ag concentrations (e.g. P4 or P5 in each group) after annealing, which is probably caused by the diffusion of Cu and Ag from within the coating to the coating surfaces (and hence formation of the aggregates discussed above).

3.2.4. Summary of surface morphology analysis

For the surface morphologies of all three groups, annealing resulted in more obvious changes to coatings containing higher Cu+Ag concentrations.

The introduction of nitrogen reduced the solubility of Cu (and Ag) in Cr; therefore, after annealing, progressively increasing numbers of aggregates formed, in direct correlation with the nitrogen flow rate increasing during coating deposition from 0 sccm to 5 sccm and then to 10 sccm.

Annealing activated the ‘transportation’ of Cu and Ag to the coating surfaces under moderately high temperature (e.g. slightly at 300 °C and more noticeably at 500 °C), which is a desirable in-service adaptive property in solid lubricating applications, because it can facilitate replenishment of the solid lubricating phases which might be consumed (e.g. worn, oxidized and/or dissolved) during service.

3.3. EDX line scan analysis

An EDX line scan across one selected aggregate from coating 10 sccm-P5-500 was carried out, with the results shown in Fig. 4. It can clearly be seen from Fig. 4 that the aggregate is (Cu, Ag)-rich. According to a further EDX point analysis of a similar aggregate, it was found that the concentrations of Cr, Cu, Ag and N in it were 33.2, 31.1, 10.5 and 25.2 at.%, respectively, with the Cu and Ag concentrations much higher than the average values measured for 10 sccm-P5-AD (as listed in table 1). Compared to the electron beam penetration depth in EDX analysis (normally in the order of a few microns, depending on the accelerating voltage and the material to be analysed), the sizes of the aggregates are relatively small (below 1 μm in diameter, as can be seen from Fig. 4). Thus there would also be some X-ray signal generated from areas surrounding (and beneath) the aggregate, being incorporated into the EDX point analysis results, making them nearer to the "average" value of the entire coating. Therefore, the real concentrations of Cu and Ag in the aggregates are likely to be even higher than the above EDX point analysis results indicate.

It is also interesting to notice that silver is more 'mobile' than copper, since - from the EDX point analysis - it can be seen that the atomic ratio of Cu:Ag is about 3:1, whereas in the as-deposited 10 sccm-P5 it is about 8:1 (Cu 23.5 at.% and Ag 3.0 at.%; Table 1). This may be related in part to the lower melting point of silver (Ag: 1234K; Cu: 1356K). However, the significantly enhanced Ag mobility is surprising (compared to the relatively small differences in homologous temperature of the two elements during annealing at 500 °C, 773K); it is clear that the transport path provided by copper allows silver to migrate to the coating surface in significant quantities even though the 'global' Ag content of the coating is low (~3 at.% or lower). According to the existing literature, in (for example) CrAgN PVD coatings with no

added Cu, the Ag concentration needs to be at least 12 at.% (more than 4× higher than in our study) to permit ‘transportation’ to the coating surface – even during annealing at quite high temperatures (e.g. 600 - 700 °C) [21] - and needs to be in excess of 20 at.% to transport sufficiently well to provide adequate solid lubricating benefits [8, 18, 20, 21, 25]. The transportation of Ag from inside to the coating surface (and subsequent aggregation) will also be a desired characteristic for antimicrobial coating applications [34, 35], particularly when the Ag aggregates are presented in nanocrystalline topography [36].

Furthermore, from the EDX line scan shown in Fig. 4, it can be seen that the Cu and Ag maxima were displaced from each other. The analysed aggregate appears Cu-rich on the left and Ag-rich on the right. In other words, after annealing, although both Cu and Ag precipitate from substitutional solid solution in Cr and transport to coating surface they are inclined to exist separately, which is in good agreement to the Ag-Cu phase diagram [37] and to first-principles calculation [38, 39] (at equilibrium silver and copper are nearly immiscible below 550K).

3.4. XRD analysis

The X-ray diffraction patterns are shown in Fig. 5.

3.4.1. The 0 sccm (nitrogen-free) control group

From the diffraction patterns of the 0 sccm control group shown in Fig. 5(a), it is clear that all of the annealed coatings (except 0 sccm-P3-500) retained the same preferred orientations as their as-deposited counterparts. Regarding 0 sccm-P3-500, it showed preferred orientation of Cr(110) rather than the Cr(211) texture of its counterparts 0 sccm-P3-AD and 0 sccm-P3-300. By comparing the patterns of the coatings annealed at 500 °C, it can also be seen that 0 sccm-P3-500 showed a transition of preferred orientation between Cr(211) and Cr(110). Moreover, distinguishable movement of shifted peaks back to their theoretical (unstrained) positions after annealing can also be seen, by comparing the diffraction patterns of as-deposited and annealed coatings. This movement means the interplanar spacings of the as-deposited coatings regressed during annealing, indicating a relaxation of compressive growth stresses. Therefore, it can be deduced that annealing probably resulted in recovery of the crystalline lattice from significant distortion (due to the supersaturated solid solution developed during sputter deposition at low temperature). Likewise, it can be deduced that the 500 °C annealing caused more lattice recovery than the 300 °C annealing, because the diffraction peaks of coatings annealed at 500 °C are more closely aligned to their theoretical values than those annealed at 300 °C, as indicated by the green lines in Fig. 5(a). Cu(111) and Cu(200) peaks were also found in the diffraction patterns of 0 sccm-P4-500 and 0 sccm-P5-500, probably because Cu precipitated from solid solution in the Cr-rich matrix and formed a separate crystalline phase after annealing at 500 °C, which is in agreement with the EDX line-scan results (section 3.3) and is further supported by the SAED patterns shown later in Fig. 9.

3.4.2. The 5 sccm group

The diffraction patterns of the 5 sccm group are shown in Fig. 5(b). The first three coatings, 5 sccm-(P1 to P3), with the same post-coat treatment (and irrespective of annealing condition: ‘AD’ or ‘300’ or ‘500’), exhibited quite similar diffraction patterns, probably due to their relatively similar chemical compositions (in contrast to P4 and P5; see Table 1). However, for each coating the phase structure changed obviously after post-coat annealing. The low and wide diffraction peaks of 5 sccm-(P1 to P3), in either ‘AD’ or ‘300’ condition, indicate an extremely distorted and supersaturated lattice structure, being amorphous or nanocrystalline (or a mixture of both). In contrast, after the 500 °C annealing, the XRD patterns of all three coatings exhibit narrower and higher-intensity peaks, indicating a phase transformation from amorphous/nanocrystalline to distinctly crystalline, with little (or no) residual lattice distortion. An apparent low and wide ‘Cr_2N(112)’ nitride peak was also found for the 500 °C annealed 5 sccm-(P1 to P3), which required further investigation (and will be discussed in the TEM analysis in section 3.5). Moreover, even after annealing at 500 °C, Cr(200) is still the observed primary lattice peak (much higher than others) indicating that, with a nitrogen concentration up to 16 at.% (or N/Cr atomic ratio up to 0.22, see Table 1), Cr exists mainly - if not entirely - as a metallic crystalline phase (with nitrogen in supersaturated interstitial solid solution). From ‘AD’ to ‘300’, the primary diffraction peaks of 5 sccm-(P1 to P3) apparently shifted from ‘nitride’ Cr_2N(112) to ‘metallic’ Cr(200). Because of the well-known high thermal stability of chromium nitride, it is unlikely that Cr_2N would somehow dissolve or decompose after 300 °C or 500 °C annealing. Therefore further investigation on the phase composition and transformation of 5 sccm-(P1 to P3), from ‘AD’ to ‘300’ to ‘500’ was required, this will also be discussed further in the TEM analysis in section 3.5.

For 5 sccm-(P4 and P5), the phase compositions of the as-deposited and 300 °C annealed coatings are quite similar, being either amorphous or nanocrystalline (or a mixture of both). However, after annealing at 500 °C, their phase structure became distinctly crystalline, with the diffraction patterns (hence phase compositions) quite similar to those of the 500 °C annealed coatings in the 10 sccm coating group. Therefore, 500 °C annealed 5 sccm-(P4 and P5) and 10 sccm-(P1 to P5) will be discussed together in the TEM analysis in section 3.5.

3.4.3. The 10 sccm group

For the diffraction patterns of the 10 sccm group shown in Fig. 5(c), it can be seen that the X-ray diffraction patterns of the as-deposited and 300 °C annealed coatings exhibited the typical featureless 'hump' of an amorphous phase. However, coatings annealed at 500 °C exhibited clear peaks of Cu(111), Cu(220), Cr(110), Cr_2N(112), which also indicated phase transformation from amorphous to crystalline due to 500 °C annealing. Further discussion will be made in the TEM analysis, as mentioned at the end of section 3.4.2 above. It needs to be mentioned that, in coatings which possess high N/Cr atomic ratios (e.g. 0.42 to 0.48, see Table 1), these ratios are in fact quite near to the stoichiometric ratio of Cr_2N - such as in 5 sccm-P5 and 10 sccm-(P1 to P4). After annealing at 500 °C, a clear Cr(110) diffraction peak was found, with its intensity around 1/3 to 1/2 of the strongest peak - Cr_2N(111), indicating that Cr remains inclined to exist as a nitrogen-supersaturated metallic phase, rather than as a stoichiometric nitride in CrCuAgN coatings, even after annealing at moderately high temperature (e.g. 500 °C).

3.4.4. Comparison among the three coating groups

From Figs. 5(b) and (c), which show the diffraction patterns of the two nitrogen-

containing groups, it can clearly be seen that diffraction patterns of coatings annealed at 300 °C exhibited wide and low-intensity peaks, similar in shape to those of their as-deposited counterparts, indicating an extremely high degree of lattice distortion. However, after 500 °C annealing, the XRD patterns of all nitrogen-containing coatings exhibited new peaks, narrower and higher in intensity - indicating a phase transformation from amorphous or nanocrystalline (or a mixture of both) to more strongly crystalline with little (or no) lattice distortion - confirming the apparent phase transformations noted in the previous surface morphology discussions of section 3.2. Moreover, these new peak positions are closely aligned to the theoretical values, indicating less lattice expansion (shift to lower angles of 2θ) or indeed contraction (shift to higher angles of 2θ), hence reduced solid solution of Cu, Ag and N in the Cr (or newly formed Cr_2N) matrix [33], which is supported by the clearly identified formation of Cu- and Ag-rich aggregates on coating surfaces (section 3.2) and the EDX line-scan data (section 3.3).

In the nitrogen-free control group, no Cu or Ag diffraction peak was found in as-deposited or annealed P1 to P3; however, Cu(200) and Ag(111) peaks were found in 0 sccm-(P4 and P5)-500, corresponding to a threshold (Cu+Ag)/Cr atomic ratio of ~0.2 (e.g. 0.22, that of 0 sccm-P4, see the red numbers in Table 1).

In the two nitrogen-containing groups, no obvious Cu peak was found in as-deposited or annealed 5 sccm-(P1 to P3); however, after annealing at 500 °C, a clear Cu(111) peak was found in 5 sccm-(P4 and P5) and in 10 sccm-(P1 to P5). By combining the chemical compositions (Table 1), it can be concluded that in nitrogen-containing coatings the (Cu+Ag+N)/Cr atomic ratio is more relevant to the separation of Cu from solid solution in Cr than the (Cu+Ag)/Cr atomic ratio. When the (Cu+Ag+N)/Cr atomic ratio is higher than ~0.5 (as is the case of P4 and P5 in the 5 sccm group and

P1 to P5 in the 10 sccm group - see the green numbers in Table 1), after annealing at 500 °C, Cu tends to separate from solid solution in Cr. In other words, the introduction of nitrogen reduces the substitutional solubility of Cu and Ag in Cr. Interestingly, Ag diffraction peaks (e.g. 111) can only be found in 500 °C annealed P4 and P5 in all three groups, indicating that the separation of Ag from solid solution in Cr is highly connected to the Cu concentration and relatively less influenced by the introduction of nitrogen (the precise mechanisms for which are under further investigation and will be published later). The (Cu+Ag)/Cr atomic ratio is therefore more important for the separation of Ag during annealing, whereas the (Cr+Ag+N)/Cr atomic ratio is more important in the case of Cu. By extracting the data of P4 in all three groups from Table 1, the threshold of the (Cu+Ag)/Cr ratio for Ag to activate the separation during annealing is around 0.2. By combining the fact the Cu and Ag aggregates were found on the surfaces of 500 °C annealed P4 and P5 in the two nitrogen-containing groups, it can be concluded that with (Cu+Ag)/Cr atomic ratio higher than 0.2 and (Cu+Ag+N)/Cr atomic ratio higher than 0.5, under moderately high temperature (e.g. 500 °C) Cu can assist Ag transportation from inside the coating onto the coating surface. It indicates that the concept of adding both Cu and Ag into nitrogen-containing chromium coatings is a feasible approach for precise tuning of nanostructure (and promotion of 'adaptive' behaviour) in solid lubricating and antibacterial applications.

3.4.5. Summary of XRD analysis

Overall, 300 °C annealing did not obviously change the phase structure of both nitrogen-free and nitrogen-containing coatings. However, annealing at 500 °C resulted in significant phase transformation in (particularly) the nitrogen-containing coatings. The newly formed Cu and Ag phases in coatings with sufficiently high Cu+Ag

concentrations were confirmed, in agreement with the surface morphology evaluation and EDX line-scan data. The formation of Ag aggregates relates to the (Cu+Ag)/Cr atomic ratio (threshold ~0.2), whereas the formation of Cu aggregates relates to the (Cu+Ag+N)/Cr atomic ratio (threshold ~0.5).

After annealing at 500 °C, with a nitrogen concentration of up to 16 at.% (or N/Cr atomic ratio up to 0.22), Cr mainly (if not entirely) continued to exist as a metallic phase. At N/Cr atomic ratios as high as 0.42-0.48 (i.e. approaching the Cr_2N stoichiometry), Cr_2N formation was promoted, but a significant proportion of nitrogen-supersaturated Cr(N) metallic phase remains in these CrCuAgN coatings.

3.5. TEM analysis

3.5.1. Coating selection for TEM analysis

Several representative nitrogen-containing coatings were chosen for TEM analysis to further investigate the phase compositions and annealing-induced phase transformations of CrCuAgN coatings. The selection of representative samples was based on the XRD analysis results (as mentioned in sections 3.4.2 and 3.4.3), which showed similar patterns for (a) the as-deposited 5 sccm-(P1 to P3); (b) the 300 °C annealed 5 sccm-(P1 to P3); (c) the 500 °C annealed 5 sccm-(P1 to P3); (d) the 500 °C annealed 5 sccm-(P4 and P5) and 10 sccm-P1 to P5. Therefore, one sample was chosen from each of the four groups above - namely: 5 sccm-P2-AD, 5 sccm-P2-300, 5 sccm-P2-500 and 10 sccm-P4-500.

SAED patterns, together with bright field (BF) and dark field (DF) images, were collected and are shown in Figs. 6 to 9, with the fitted indices of corresponding crystallographic planes marked on the SAED patterns. The sampled diffraction point (or part of a diffraction ring) for dark field imaging are indicated using small black circles - as can be seen from the SAED patterns in each of the abovementioned figures.

3.5.2. 5 sccm-P2-AD

The SAED pattern, BF and DF images for 5 sccm-P2-AD, are shown in Fig. 6. From the SAED pattern in Fig. 6(a), discontinuous diffraction rings with a small number of spots (as indicated by the yellow arrows) can be seen. The diffraction rings exhibit relatively narrow width and sharp boundaries (compared to the typical wide and blurred diffraction rings of an amorphous phase), indicating that the phase was not completely amorphous. However, it was also not a typical nanocrystalline diffraction

pattern, an excellent example of which is shown later in Fig. 8(b). Therefore, the phase is probably ultra-fine nanocrystalline (probably smaller than a few nanometers), which is also the reason why it is undetectable by XRD. The existence of ultra-fine Cr nanocrystallites can be verified by the corresponding BF and DF images, as shown at relatively low magnification in Figs. 6(b) and (c), and the same selected area shown at higher magnification in Fig. 6(d) and (e), respectively. From the BF and DF images, especially the high magnification DF image shown in Fig. 6(e), it can be seen that the white 'dots' are of sizes ranging from less than 1nm up to ~10nm - and are Cr nanocrystallites. Moreover, the rings are discontinuous (e.g. the (110) plane diffraction ring in Fig. 6(a)), indicating that these ultra-fine nanocrystallites are not randomly oriented. In other words, they possess preferential orientations (but more than one; otherwise discrete spots - rather than discontinuous rings – will be observed). Furthermore, the SAED pattern shows a very good fit to the calculated diffraction rings of bcc-Cr - rather than those of the Cr_2N ceramic phase (as the abovementioned XRD data seemed to suggest). No Cu or Ag patterns were found, indicating that they most probably existed in substitutional solid solution in the ultra-fine nanocrystalline Cr phase. As alluded to in section 3.4.3, despite the existence of 16 at.% nitrogen in the as-deposited 5 sccm-P2 coating, the main constituent is an ultra-fine grained Cr-rich metallic phase (with supersaturated nitrogen in interstitial solid solution), rather than a ceramic nitride. Although for 5 sccm-P2-AD the wide, low-intensity peak in the XRD pattern roughly matched with the expected position of the $Cr_2N(112)$ reflection, it probably merely indicated the existence of a ultra-fine nanocrystalline phase (as confirmed by SAED pattern), since no existence of nitrides could be confirmed by TEM for this coating.

3.5.3. 5 sccm-P2-300

The SAED pattern, BF and DF images for 5 sccm-P2-300 are shown in Fig. 7. Clear diffraction spots around the rings (Fig. 7(a)) were revealed, with the discontinuous diffraction rings found in 5 sccm-P2-AD having faded, but not totally disappeared - indicating a mixed structure of ultra-fine and nanocrystalline phases. The BF and DF images (from the same area), as shown in Figs. 7(b), (c) and Figs. (d), (e) respectively, at relatively low and at higher magnification, suggest that the nanostructure of 5 sccm-P2-300 remains quite similar to that of 5 sccm-P2-AD. A slight difference after 300 annealing is seen in the higher number of relatively large nanocrystallites visible, compared to 5 sccm-P2-AD (e.g. those of the order of several nanometers in diameter, comparing Fig. 6(e) with Fig. 7(e)), which is indicative of a small amount of annealing-induced grain growth. The pattern again correlates well to the calculated diffraction ring positions for bcc-Cr metal. As for 5 sccm-P2-300, no Cu or Ag pattern was found; therefore, by combining the EDX and XRD analyses, it can be deduced that 5 sccm-P2-300 was mainly composed of ultra-fine to nanocrystalline metallic Cr, with Cu and Ag in substitutional solid solution and nitrogen in supersaturated interstitial solid solution (similar to 5 sccm-P2-AD, except grain size). The three alloying elements, Cu, Ag and N, either co-exist in one metallic Cr-rich phase, or may exist separately, e.g. nanocrystalline Cr(Cu, Ag) and Cr(N); however neither scenario can be unambiguously determined from the present data (further investigation of the alloying mechanisms is also ongoing and will again be published later). No existence of nitride phases was found by TEM in 5 sccm-P2-300.

3.5.4. 5 sccm-P2-500

The SAED pattern, BF and DF images for 5 sccm-P2-500 are shown in Fig. 8. The

SAED pattern (Fig. 8(a)) showed a typical nanocrystalline electron diffraction pattern, and it was perfectly-fitted to the calculated diffraction rings of bcc-Cr. A diffuse ring was also found and marked by black arrows in Fig. 8(a), which indicated the co-existence of an amorphous phase. Because Cr was confirmed to exist as nanocrystallites, the amorphous phase was most probably composed of Cu, Ag and N (and possibly Cr as well, since it is known that up to 40 at.% Cr can co-exist in an amorphous Cu phase for sputtered PVD Cr-Cu coatings deposited at low temperature [26]). Similar to the 5 sccm-P2-300 sample, no existence of nitrides could be confirmed by TEM for the P2-500 coating. The sizes of the nanocrystallites are relatively evenly distributed (compared to those of 5 sccm-P2-AD and 5 sccm-P2-300) in a range of 10nm to 20nm, as can be seen from Figs. 8(d) and (e). Particularly, clear moiré fringes (under this magnification, the only possible cause of such fringes is the interference of crossed lattice planes) were observed in Fig. 8(e), which further confirmed that the particles found were crystalline rather than amorphous.

3.5.5. 10 sccm-P4-500

i). 10 sccm-P4-500: a SAED pattern and BF image

The SAED pattern and BF image of 10 sccm-P4-500 are shown in Fig. 9. From the SAED pattern (Fig. 9(a)), it can be seen from the calculated diffraction rings (solid lines in different colours) of Cr, Cu and Cr_2N that a large number of them are closely overlapped, and hence difficult to distinguish without ambiguity. However, the existence of nanocrystalline Cr_2N can be easily confirmed according to the clear dotted diffraction rings (similar to the features of Fig. 8(a), indicating a nanocrystalline structure based on the discussion above) of low-index planes, e.g. Cr_2N(101), (110) and (112). The existence of nanocrystalline Cr and Cu can also be

confirmed by Cr(110), Cr(200) and Cu(200), respectively, because of the relatively large and distinguishable distances of these diffraction rings from others in Fig. 9(a). However, no Ag diffraction rings or spots can be confirmed by our TEM analysis. One (likely) reason is that every Ag diffraction ring is so close to one or more diffraction rings of Cr, Cu and/or Cr_2N that they could not be separately resolved. Other possible reasons are the relatively low concentration of Ag in all coatings, and its preferential transportation to the coating surface during 500 °C annealing (as confirmed in Fig. 4), resulting in very little Ag remaining in the area from which this particular TEM sample was extracted.

ii). 10 sccm-P4-500: three DF images of a same selected area

Three DF images of 10 sccm-P4-500 are shown in Fig. 10; these were obtained by choosing different sizes and parts of the SAED pattern shown in Fig. 9(a), with the corresponding sectors of the diffraction pattern indicated using black, red and green circles in Fig. 9(a), respectively.

Fig. 10(a), with the corresponding diffraction pattern indicated by a black circle in Fig. 9(a), shows a number of nanocrystallites with sizes ranging from several nanometers to several tens of nanometers. Four relatively large grains are labelled 1-4, respectively, as shown in Fig. 10.

After choosing a smaller objective aperture, shown using a red circle in Fig. 9(a), the DF image changed to that shown in Fig. 10(b), imaged from the same area as in Fig. 10(a). It can be seen that grain 1 and 2 are still visible in Fig. 10(b), however grains 3 and 4 “disappeared”. Because Cr(110) exhibited the brightest diffraction ring (see Fig. 9(a)) and the centre of the red circle is on the Cr(110) diffraction ring, it may be deduced that grain 1, which is the largest and brightest grain in Fig. 10(b), is probably

a nanocrystalline Cr grain, with the (110) plane (or equivalent planes from the {110} family) perpendicular to the TEM sample foil (no stage tilt was applied when obtaining the SAED patterns and DF images). Grain 2, however, could be a nanocrystallite corresponding to Cu(111), Cr_2N(111), Cr_2N(200) or Cr_2N(201) orientations, and could not be fully confirmed, due to the nearly overlapped diffraction rings and relatively large objective aperture (although the smallest objective aperture in the TEM instrument had been used for Figs. 10(b) and (c)).

By moving the objective aperture to another area (shown using the green circle in Fig. 9(a)) a third DF image, Fig. 10(c), was obtained. This time only one diffraction ring (with two diffraction spots along it) was included inside the objective aperture, which is Cr_2N(112) - see Fig. 9(a). From Fig. 10(c), it can be seen that the "disappeared" grains 3 and 4 became visible once more, which confirms these to be Cr_2N nanocrystallites - with plane indices belonging to the {112} family.

3.5.6. Summary of TEM analyses

Overall, TEM analyses of 5 sccm-P2-(AD, 300 and 500) reveal phase transformations from the original ultra-fine nanocrystalline Cr-based solid solution (5 sccm-P2-AD; Cu and Ag in substitutional solid solution and N in supersaturated interstitial solid solution), to a mixture of nanocrystalline Cr and ultra-fine nanocrystalline Cr-based solid solution after 300 °C annealing (5 sccm-P2-300; similar solid solutions as the as-deposited coating), then to a mixture of nanocrystalline Cr and an amorphous phase consisting of Cu, Ag, N (and possibly also Cr) after 500 °C annealing (5 sccm-P2-500). The formation of an amorphous phase (Cu, Ag, N and/or with Cr) originating from the nanocrystalline Cr-based solid solution, possibly results from the low miscibility of Cu with Ag [37-39] (and also of Cu with Cr –and/or Ag with Cr

[37]), together with the non-nitride forming characteristics of Cu and Ag. Because Fig. 5(b) shows that 5 sccm-(P1 to P3) exhibited quite similar XRD patterns to each other - whether in the as-deposited state, or in either of the two annealed states - it can be deduced that similar phase transformations occurred for each of 5 sccm-(P1 to P3).

From the XRD and TEM analysis of 5 sccm-P2-(AD, 300 and 500), It can also be seen that, for nitrogen-containing coatings with nitrogen content up to 16 at.% (and/or N/Cr atomic ratio up to 0.22, see Table 1.), chromium exists as a metallic supersaturated interstitial solid solution with nitrogen, even after 300 °C and 500 °C annealing.

After annealing, Cu exists not only on the coating surface, but also inside the coating (e.g. in solid solution for 5 sccm-P2-300, in an amorphous state for 5 sccm-P2-500, or as nanocrystallites in 10 sccm-P4-500), rather than being fully transported to the coating surfaces - indicating the dependence of this "transportation" on annealing duration. Moreover, annealing at 500 °C caused more and larger Cu-Ag aggregates to be formed on the coating surface than did annealing at 300 °C, indicating the (not unexpected) dependence of the Cu (and Ag) transportation speed on temperature. Furthermore, increasing nitrogen concentration caused larger Cu (and Ag) aggregates to form on the coating surface, indicating the dependence also of the Cu (and Ag) transportation (different from the influencing factors of the separation of Cu and/or Ag from solid solution in Cr, which are (Cu+Ag+N)/Cr and (Cu+Ag)/Cr atomic ratios, respectively) on nitrogen concentration. Considering the apparent dependence of Cu and Ag transportation on the 'global' Cu+Ag concentration, a conclusion can be drawn that the transportation of Cu and Ag to the surface depends on annealing temperature, annealing duration, nitrogen concentration and overall Cu+Ag concentration. In other words - by appropriate design - the transportation of Cu (and

particularly Ag) can be tuned for specific applications in order to obtain both the required functionality (such as solid lubrication) and an optimised service life in, for example, high temperature (or cyclic temperature) tribological or antimicrobial service conditions, as stated in section 3.3.

3.6. Coefficients of friction

3.6.1 Scratch test

Scratch test results showing the CoF of the AISI 316L substrate, and 5 sccm-P4-(AD, 300 and 500) are shown in Fig. 11. It can be clearly seen that CrCuAgN coatings exhibited significantly lower CoF than the AISI 316L substrate. Moreover, for the same coating, annealing at higher temperature resulted in lower CoF in the scratch test. Particularly, the average CoF of 5 sccm-P4-500 was only 0.14, reduced by more than 50% compared to that of the AISI 316L substrate (~0.31). The corresponding CoFs of as-deposited and annealed coatings are in good agreement with the morphology and nanostructure discussions made in sections 3.1 to 3.5.

3.6.2 Reciprocating sliding wear test at room and elevated temperature

The results of reciprocating sliding wear tests - at room temperature (~20 °C), 300 °C and 500 °C, respectively - of polished AISI 316L substrate and 5 sccm-P4-AD, with an alumina ball counterface, are shown in Fig. 12. It can be seen that the CoF of 5 sccm-P4-AD decrease significantly as the ambient temperature increases, from an average of ~0.77 (tested at RT) to as low as ~0.40 (tested at 500 °C). Compared to the average CoF of the polished AISI 316L substrate (~0.83), the CoF of 5 sccm-P4-AD at medium high temperature (500 °C) is reduced by more than 50%. It can also be seen that the CoF at 500 °C is much more stable – and reduces slowly as the test carries on, indicating the stability of the solid lubricating performance under medium high temperature for the CrCuAgN coatings. The tribological properties of CrCuAgN coatings in this study are in good agreement with those of the CrN-Ag coatings (with more than 20 at.% of Ag) studied by Mulligan, et al [18-20].

4. Conclusions

The effects of annealing on the fracture sections, surface morphologies, phase compositions and nanostructure of CrCuAgN PVD coatings were comprehensively investigated. The following conclusions can be drawn:

i) Annealing altered the coating fracture section appearance and surface morphology; as might typically be expected, the higher the annealing temperature, the more obvious are the changes occurring to the coating nanostructure, phase composition and (somewhat more importantly) surface morphology/chemical composition. Copper- and silver-rich aggregates formed on the surfaces of nitrogen-containing coatings after annealing, the number and size of which increased with increasing Cu+Ag concentration and/or annealing temperature. The number and size of the surface aggregates were also influenced by the nitrogen flow rate, probably due to the incorporation of nitrogen reducing the solubility of Cu and Ag in Cr, or Cr_2N (where formed).

ii) In coatings with a nitrogen concentration of up to 16 at.% (N/Cr atomic ratio up to 0.22), a metallic Cr solid solution with supersaturated interstitial nitrogen remained present, even after post-coat annealing at 300 °C and 500 °C. At higher N/Cr atomic ratios of 0.42-0.48 (i.e. approaching Cr_2N stoichiometry), chromium was still inclined to partially exist in the CrCuAgN coatings as a metallic interstitial solid solution with nitrogen, rather than as a ceramic nitride phase, even after annealing at 500 °C.

iii) The formation of Ag aggregates relates primarily to the (Cu+Ag)/Cr atomic ratio in the coating, whereas the formation of Cu aggregates relates primarily to the (Cu+Ag+N)/Cr atomic ratio. In CrCuAgN coatings with (Cu+Ag)/Cr and

(Cu+Ag+N)/Cr atomic ratios higher than 0.2 and 0.5, respectively, under relatively high temperature (e.g. 500 °C), Cu can assist Ag to be transported from within the coating to the coating surface - and with surprisingly enhanced Ag mobility (much higher than Cu), most probably due to formation of a transport path by the development of intercolumnar copper-rich phases, which enable the silver to migrate efficiently. Moreover, after annealing, although both Cu and Ag precipitate from substitutional solid solution in Cr (and are then transported to coating surface), they are inclined to exist separately.

iv) The transportation of Cu and Ag to the surface depends on annealing temperature, annealing duration, nitrogen concentration and 'global' Cu+Ag concentration. This provides a possibility to tailor coatings with desired functionalities and properties for specific applications.

v) A significant decrease in the coefficients of friction, over 50% compared to that of the substrate (from 0.31 to 0.14 with diamond indenter, and from 0.83 to 0.40 with alumina ball, respectively) was obtained for the CrCuAgN coatings, showing effective solid lubricating behaviour.

vi) Furthermore, almost all of the available literature on MeN:Ag PVD coatings reveals the silver to precipitate as separate, isolated particles, with little or no migration path available - whereas the incorporation of copper (which, it is known, tends to precipitate as an intergranular/intercolumnar phase) appears to be a powerful strategy to enhance Ag mobility at low concentration (from ~20 at.% in the literature for no added Cu to ~3 at.% in this study) in such coatings under moderately high service temperature (and/or by coating pre-conditioning through careful post-coat annealing). Therefore, the results of the present study indicate that the concurrent addition of both Cu and Ag (in appropriate concentrations) to

PVD nitrogen-containing chromium coatings is a viable method to promote adaptive behaviour - and to permit the development of ‘self-replenishing’ thin film architectures for antimicrobial and solid lubricating coating applications.

Acknowledgements

We gratefully acknowledge funding support from the UK Technology Strategy Board (now Innovate UK) and the Engineering & Physical Sciences Research Council (TS/J000949/1). Thanks also to Le Ma and Itzel Castillo-Muller for assistance with high-temperature tribometry.

References

[1] S. Ma, D. Ma, Y. Guo, B. Xu, G. Wu, K. Xu, P.K. Chu, Synthesis and characterization of super hard, self-lubricating Ti–Si–C–N nanocomposite coatings, Acta Materialia, 55 (2007) 6350-6355.
[2] P. Basnyat, B. Luster, Z. Kertzman, S. Stadler, P. Kohli, S. Aouadi, J. Xu, S. Mishra, O. Eryilmaz, A. Erdemir, Mechanical and tribological properties of CrAlN-Ag self-lubricating films, Surface and Coatings Technology, 202 (2007) 1011-1016.
[3] V. Ezirmik, E. Senel, K. Kazmanli, A. Erdemir, M. Ürgen, Effect of copper addition on the temperature dependent reciprocating wear behaviour of CrN coatings, Surface and Coatings Technology, 202 (2007) 866-870.
[4] H.C. Barshilia, N. Selvakumar, B. Deepthi, K. Rajam, A comparative study of reactive direct current magnetron sputtered CrAlN and CrN coatings, Surface and Coatings Technology, 201 (2006) 2193-2201.
[5] R. Zhang, S. Sheng, S. Veprek, Stability of Ti–B–N solid solutions and the formation of nc-TiN/a-BN nanocomposites studied by combined ab initio and thermodynamic calculations, Acta Materialia, 56 (2008) 4440-4449.
[6] T. Elangovan, P. Kuppusami, R. Thirumurugesan, C. Sudha, E. Mohandas, D. Mangalaraj, A Study on the Influence of Copper Content in CrN/Cu Nanocomposite Thin Films Prepared by Pulsed DC Magnetron Sputtering, Journal of Nanoscience and Nanotechnology, 9 (2009) 5436-5440.
[7] L. Incerti, A. Rota, S. Valeri, A. Miguel, J. García, R. Rodríguez, J. Osés, Nanostructured self-lubricating CrN-Ag films deposited by PVD arc discharge and magnetron sputtering, Vacuum, 85 (2011) 1108-1113.
[8] P. Papi, C. Mulligan, D. Gall, CrN-Ag Nanocomposite Coatings: Control of Lubricant Transport by Diffusion Barriers, Thin solid films, DOI (2012) 211-217.
[9] O. Jimenez, M. Audronis, M. Baker, A. Matthews, A. Leyland, Structure and mechanical properties of nitrogen-containing Zr–Cu based thin films deposited by pulsed magnetron sputtering, Journal of Physics D: Applied Physics, 41 (2008) 155301.
[10] J.L. Endrino, J.J. Nainaparampil, J.E. Krzanowski, Microstructure and vacuum tribology of TiC–Ag composite coatings deposited by magnetron sputtering-pulsed laser deposition, Surface and Coatings Technology, 157 (2002) 95-101.
[11] Y. Pei, D. Galvan, J.T.M. De Hosson, Nanostructure and properties of TiC/aC: H composite coatings, Acta Materialia, 53 (2005) 4505-4521.
[12] L. Isaeva, J. Sundberg, S. Mukherjee, C.J. Pelliccione, A. Lindblad, C.U. Segre, U. Jansson, D. Sarma, O. Eriksson, K. Kádas, Amorphous W–S–N thin films: The atomic structure behind ultra-low friction, Acta Materialia, 82 (2015) 84-93.
[13] Y. Wang, J. Wang, G. Zhang, L. Wang, P. Yan, Microstructure and tribology of TiC (Ag)/aC: H nanocomposite coatings deposited by unbalanced magnetron sputtering, Surface and Coatings Technology, 206 (2012) 3299-3308.
[14] A. Voevodin, J. Hu, J. Jones, T. Fitz, J. Zabinski, Growth and structural characterization of yttria-stabilized zirconia–gold nanocomposite films with improved toughness, Thin solid films, 401 (2001) 187-195.
[15] C. Muratore, A. Voevodin, J. Hu, J. Zabinski, Tribology of adaptive nanocomposite yttria-stabilized zirconia coatings containing silver and molybdenum from 25 to 700 C, Wear, 261 (2006) 797-805.
[16] C. Muratore, J. Hu, A. Voevodin, Adaptive nanocomposite coatings with a titanium nitride diffusion barrier mask for high-temperature tribological applications, Thin solid films, 515 (2007) 3638-3643.
[17] K. Kutschej, C. Mitterer, C.P. Mulligan, D. Gall, High-Temperature Tribological Behavior of CrN-Ag Self-lubricating Coatings, Advanced Engineering Materials, 8 (2006) 1125-1129.
[18] C. Mulligan, T. Blanchet, D. Gall, CrN–Ag nanocomposite coatings: High-temperature tribological response, Wear, 269 (2010) 125-131.
[19] C. Mulligan, T. Blanchet, D. Gall, CrN–Ag nanocomposite coatings: Tribology at room temperature and during a temperature ramp, Surface and Coatings Technology, 204 (2010) 1388-1394.
[20] C. Mulligan, T. Blanchet, D. Gall, Control of lubricant transport by a CrN diffusion barrier layer during high-temperature sliding of a CrN–Ag composite coating, Surface and Coatings Technology, 205 (2010) 1350-1355.
[21] C. Mulligan, D. Gall, CrN–Ag self-lubricating hard coatings, Surface and Coatings Technology, 200 (2005) 1495-1500.
[22] P. Kuppusami, T. Elangovan, S. Murugesan, R. Thirumurugesan, S. Khan, R. George, R.

Ramaseshan, R. Divakar, E. Mohandas, D. Mangalaraj, Microstructural, nanomechanical and antibacterial properties of magnetron sputtered nanocomposite thin films of CrN/Cu, Surface Engineering, 28 (2011) 134-140.
[23] A. Öztürk, K. Ezirmik, K. Kazmanlı, M. Ürgen, O. Eryılmaz, A. Erdemir, Comparative tribological behaviors of TiN, CrN and MoNCu nanocomposite coatings, Tribology International, 41 (2008) 49-59.
[24] C. Mulligan, T. Blanchet, D. Gall, CrN–Ag nanocomposite coatings: Effect of growth temperature on the microstructure, Surface and Coatings Technology, 203 (2008) 584-587.
[25] C. Mulligan, P. Papi, D. Gall, Ag transport in CrN-Ag nanocomposite coatings, Thin solid films, DOI (2012) 6774-6779.
[26] H. Holleck, Metastable coatings—prediction of composition and structure, Surface and Coatings Technology, 36 (1988) 151-159.
[27] M. Baker, P. Kench, M. Joseph, C. Tsotsos, A. Leyland, A. Matthews, The nanostructure and mechanical properties of PVD CrCu (N) coatings, Surface and Coatings Technology, 162 (2003) 222-227.
[28] J.W. Lee, Y.C. Kuo, Y.C. Chang, Microstructure and mechanical properties of pulsed DC magnetron sputtered nanocomposite Cr–Cu–N thin films, Surface and Coatings Technology, 201 (2006) 4078-4082.
[29] A. Leyland, A. Matthews, On the significance of the H/E ratio in wear control: a nanocomposite coating approach to optimised tribological behaviour, Wear, 246 (2000) 1-11.
[30] A. Leyland, A. Matthews, Design criteria for wear-resistant nanostructured and glassy-metal coatings, Surface and Coatings Technology, 177-178 (2004) 317-324.
[31] M. Baker, P. Kench, C. Tsotsos, P. Gibson, A. Leyland, A. Matthews, Investigation of the nanostructure and wear properties of physical vapor deposited CrCuN nanocomposite coatings, Journal of Vacuum Science & Technology A: Vacuum, Surfaces, and Films, 23 (2005) 423-433.
[32] M. Joseph, C. Tsotsos, M. Baker, P. Kench, C. Rebholz, A. Matthews, A. Leyland, Characterisation and tribological evaluation of nitrogen-containing molybdenum–copper PVD metallic nanocomposite films, Surface and Coatings Technology, 190 (2005) 345-356.
[33] X. Liu, J. Kavanagh, A. Matthews, A. Leyland, The combined effects of Cu and Ag on the nanostructure and mechanical properties of CrCuAgN PVD coatings, Surface and Coatings Technology, 284 (2015) 101-111.
[34] P. Kelly, H. Li, K.A. Whitehead, J. Verran, R. Arnell, I. Iordanova, A study of the antimicrobial and tribological properties of TiN/Ag nanocomposite coatings, Surface and Coatings Technology, 204 (2009) 1137-1140.
[35] J. Zhao, H. Feng, H. Tang, J. Zheng, Bactericidal and corrosive properties of silver implanted TiN thin films coated on AISI317 stainless steel, Surface and Coatings Technology, 201 (2007) 5676-5679.
[36] K. Dunn, V. Edwards-Jones, The role of Acticoat™ with nanocrystalline silver in the management of burns, Burns, 30 (2004) S1-S9.
[37] T.B. Massalski, H. Okamoto, P. Subramanian, L. Kacprzak, W.W. Scott, Binary alloy phase diagrams, American Society for Metals Metals Park, OH1986.
[38] V. Ozoliņš, C. Wolverton, A. Zunger, Cu-Au, Ag-Au, Cu-Ag, and Ni-Au intermetallics: First-principles study of temperature-composition phase diagrams and structures, Physical Review B, 57 (1998) 6427-6443.
[39] J. Sanchez, J. Stark, V. Moruzzi, First-principles calculation of the Ag-Cu phase diagram, Physical Review B, 44 (1991) 5411-5418.

Fig. 1. Schematic drawing of (a) target-substrate arrangement in deposition chamber and (b) plan-view of Cu-Ag target.

Fig. 2. Fracture section SEM micrographs of (a) nitrogen-free control group, (b) 5 sccm group and (c) 10 sccm group, in which "AD" means "as deposited", "300" means annealed at 300 °C for 2 hours, and "500" means annealed at 500 °C for 2 hours.

Fig. 3. Oblique-view coating surface SEM micrographs of (a) nitrogen-free control group, (b) 5 sccm group and (c) 10 sccm group, with Cu and/or Ag aggregates indicated by the red circles.

Fig. 4. EDX line scan results of an aggregate on the surface of sample 10 sccm-P5-500.

Fig. 5. X-ray diffraction patterns of the as-deposited and annealed coatings, (a) nitrogen-free control group, (b) 5 sccm group and (c) 10 sccm group.

Fig. 6. Plane-section TEM images and SAED pattern of 5 sccm-P2-AD, (a) SAED pattern; (b) BF image at low magnification; (c) DF image at low magnification, same area as (b), with its corresponding diffraction point (part of the (110) ring) shown in the black circle in (a); (d) BF image of the selected area shown in (b) at high magnification; (e) DF image of the selected area shown in (c) at high magnification, which is also the same feature as the one shown in (d).

Fig. 7. Plane-section TEM images and SAED pattern of 5 sccm-P2-300, (a) SAED pattern; (b) BF image at low magnification; (c) DF image at low magnification, same area as (b), with its corresponding diffraction point (part of the dashed (110) ring) shown in the black circle in (a); (d) BF image of the selected area shown in (b) at high magnification; (e) DF image of the selected area shown in (c) at high magnification, which is also the same feature as the one shown in (d).

Fig. 8. Plane-section TEM images and SAED pattern of 5 sccm-P2-500, (a) SAED pattern; (b) BF image at low magnification; (c) DF image at low magnification, same area as (b), with its corresponding diffraction point (part of the dashed (110) ring) shown in the black circle in (a); (d) BF image at high magnification; (e) BF image of another area at high magnification, with clear moiré fringes as indicated in red circles.

Fig. 9. Plane-section TEM images and SAED pattern of 10 sccm-P4-500, (a) SAED pattern and (b) BF image at low magnification.

Fig. 10. DF images of 10 sccm-P4-500, with their corresponding diffraction pattern shown in Fig. 9, (a) the large black circle, which contains (b), (c); (b) the small red circle, in which are parts of the diffraction rings belonged to Cr(110), Cu(111), Cr2N(111), Cr2N(200) and Cr2N(201), with Cr(110) being the brightest; (c) the small green circle, in which are two diffraction points along the Cr2N(112) diffraction ring.

Figure 11. Evaluation at room temperature of coefficients of friction for the AISI 316L substrate and 5 sccm-P4-(AD, 300 and 500). Tests performed using a Rockwell C diamond stylus and 20N constant load.

Figure 12. Evaluation of coefficients of friction at room temperature (RT), 300 °C and 500 °C, for the AISI 316L substrate and 5 sccm-P4-AD. Tests performed with an alumina ball (6.35 mm in diameter) counterface; normal load, sliding distance and frequency being 1 N, 1 mm and 1 Hz, respectively.

Table

Table 1. Thickness, coating deposition rate, elemental composition of the as-deposited coatings

N_2 flow rate (sccm)	Posi-tion	Thick-ness (µm)	Deposition rate (nm/min)	at% (±0.5) (Nitrogen: ± 1.5 at%) N	Cr	Cu	Ag	N/Cr ratio	(Cu+Ag) /Cr ratio	(Cu+Ag+N) /Cr ratio
0 (Nitrogen free)	1	3.9	43	--	92.7	5.4	1.9	--	0.08	--
	2	4.5	50	--	90.7	7.1	2.2	--	0.10	--
	3	3.6	40	--	87.3	9.8	2.9	--	0.15	--
	4	3.1	34	--	81.8	16.4	1.8	--	0.22	--
	5	3.5	39	--	67.3	30.2	2.5	--	0.49	--
5	1	3.7	41	16	76.6	5.0	2.2	0.21	0.09	0.30
	2	4.1	46	16	74.9	6.5	2.3	0.21	0.12	0.33
	3	3.7	41	16	73.1	8.5	2.0	0.22	0.14	0.36
	4	2.7	30	18	65.1	15.3	2.0	0.28	0.27	0.54
	5	2.7	30	22	47.9	26.3	3.6	0.46	0.62	1.08
10	1	3.6	40	27	65.0	5.1	2.5	0.42	0.12	0.53
	2	4.0	44	28	64.2	5.6	2.4	0.44	0.12	0.56
	3	3.3	37	29	60.5	7.5	2.8	0.48	0.17	0.65
	4	2.9	32	26	59.8	12.9	1.6	0.44	0.24	0.68
	5	2.8	31	28	45.5	23.5	3.0	0.62	0.58	1.20

Figure 1

Click here to download high resolution image

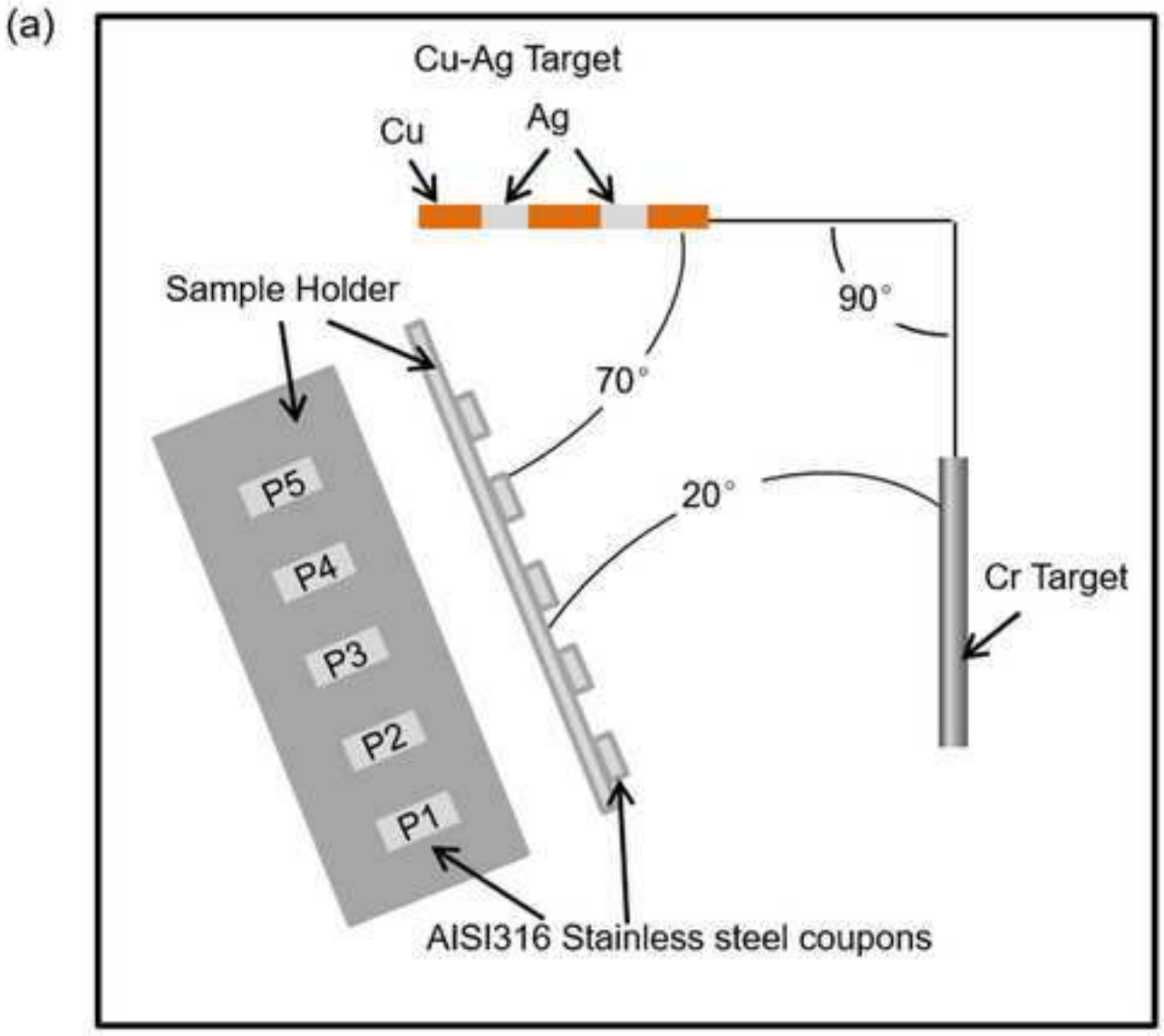

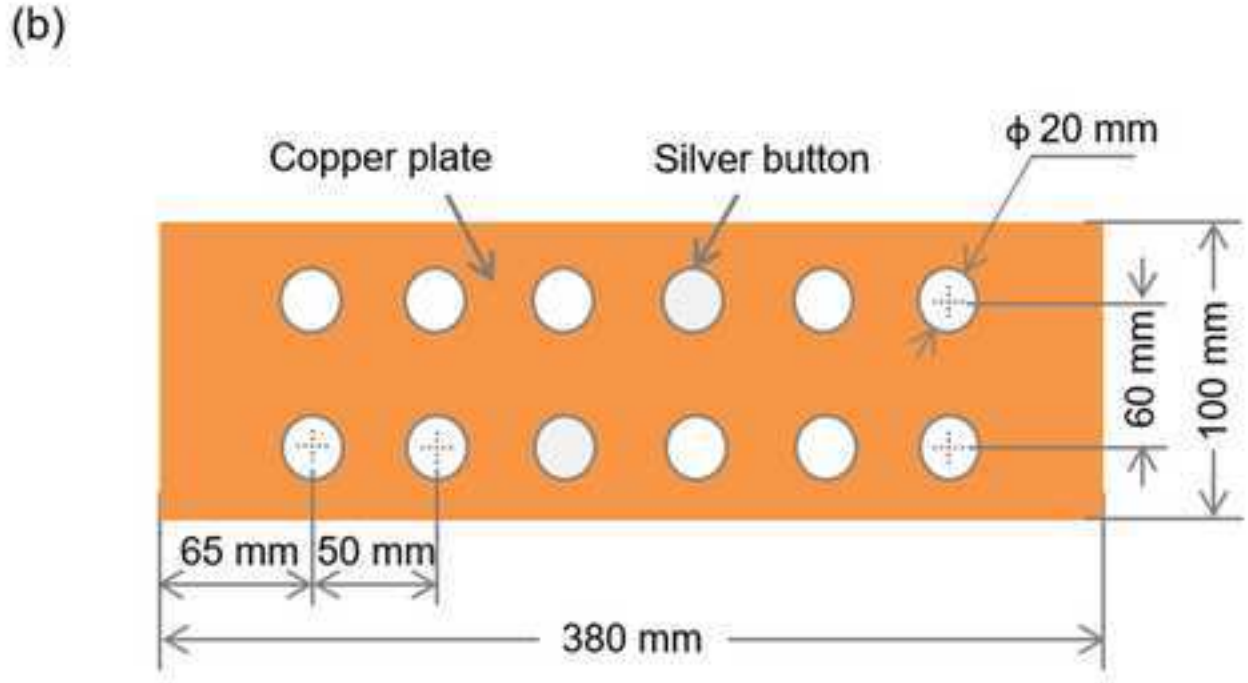

Figure 2

Click here to download high resolution image

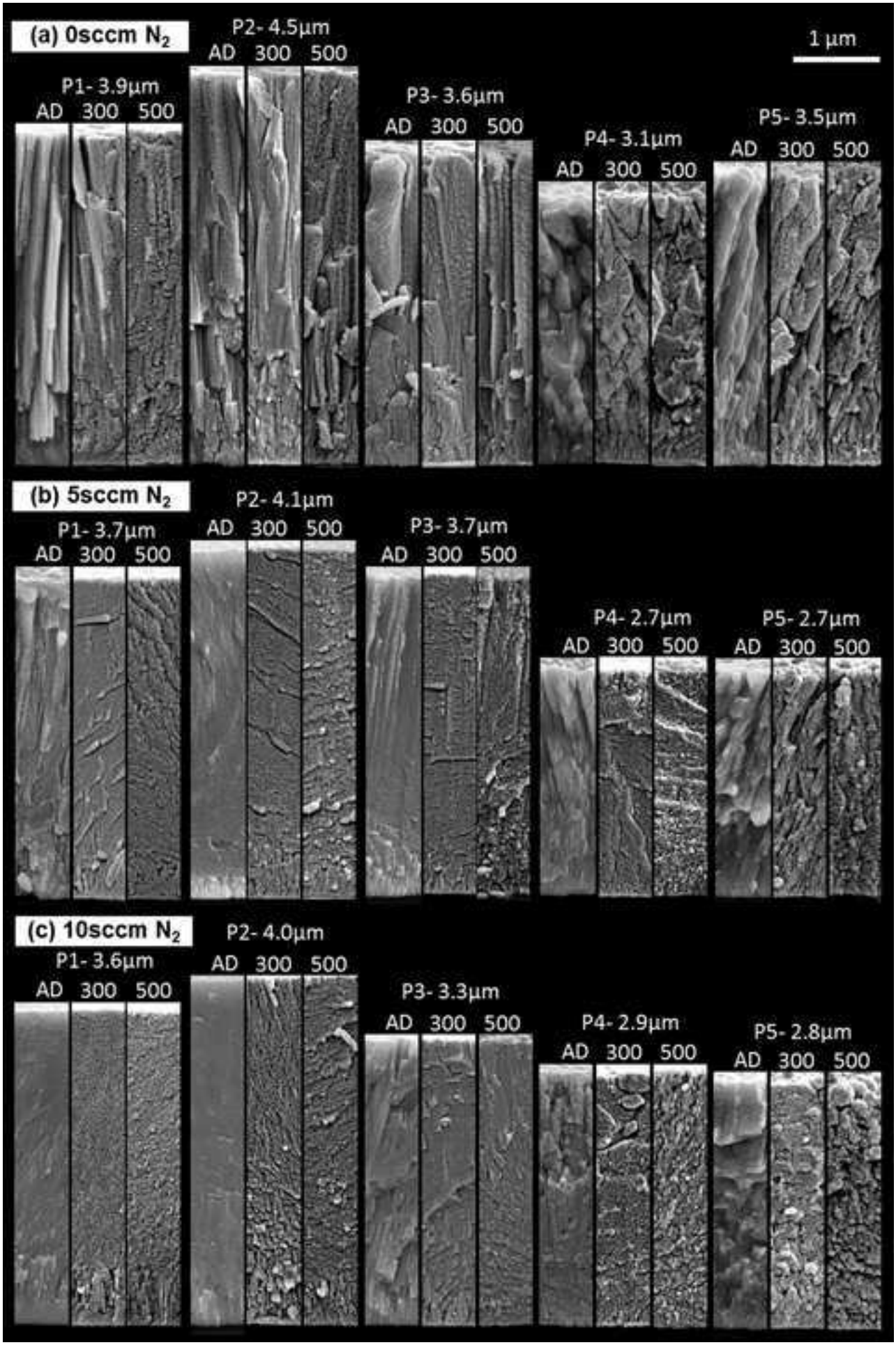

Figure 3a

Click here to download high resolution image

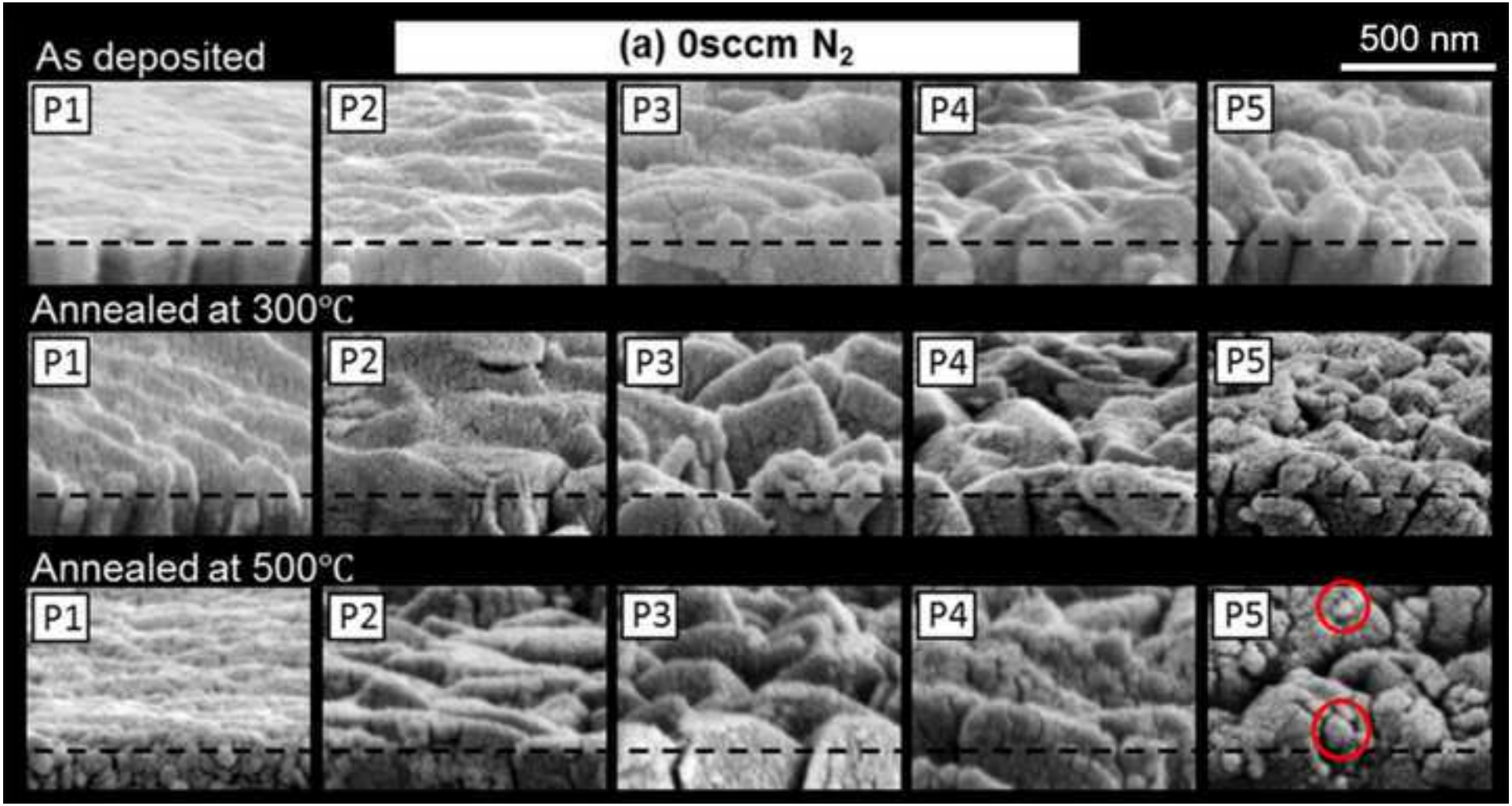

Figure 3b

Click here to download high resolution image

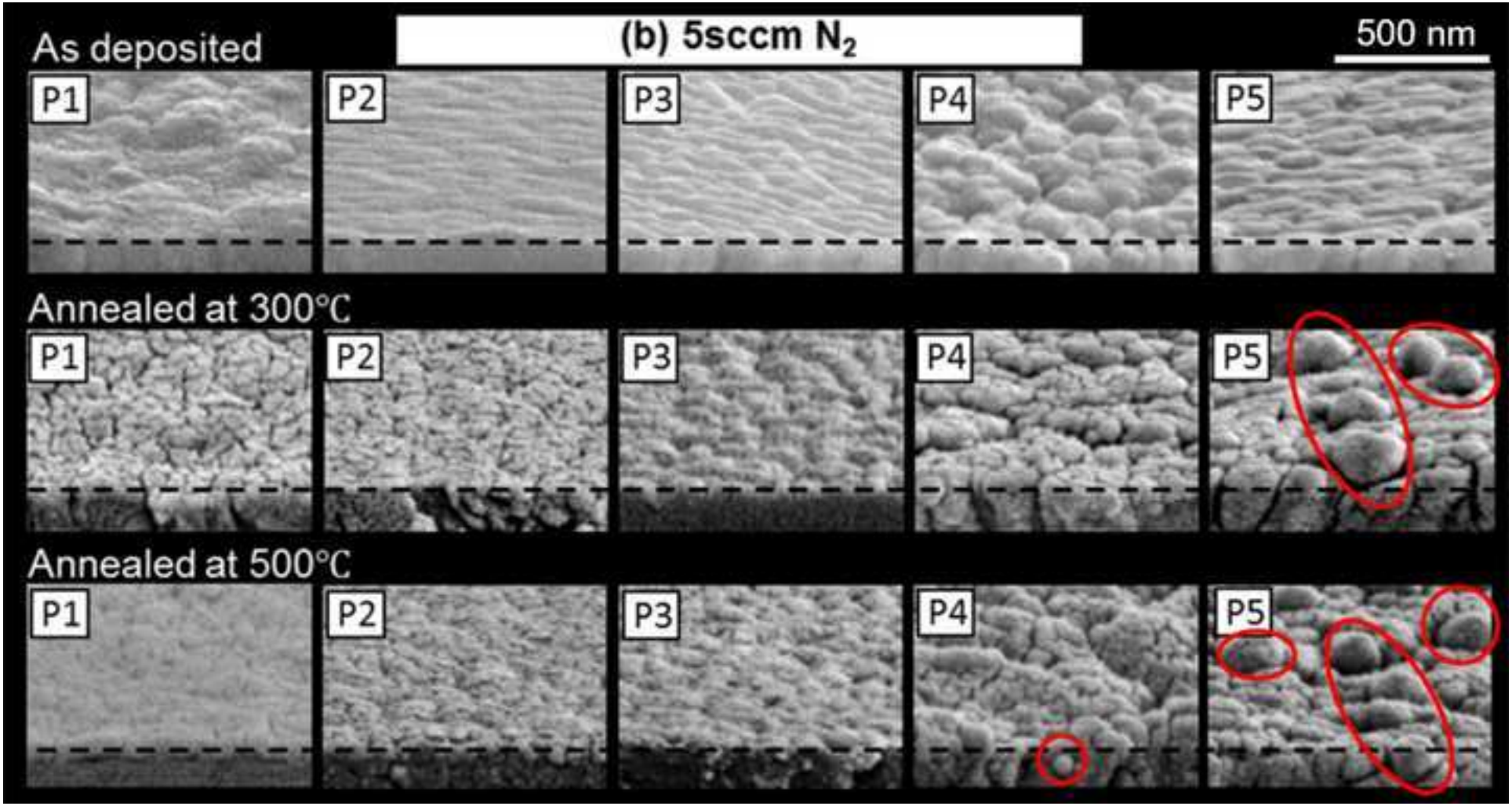

Figure 3c

Click here to download high resolution image

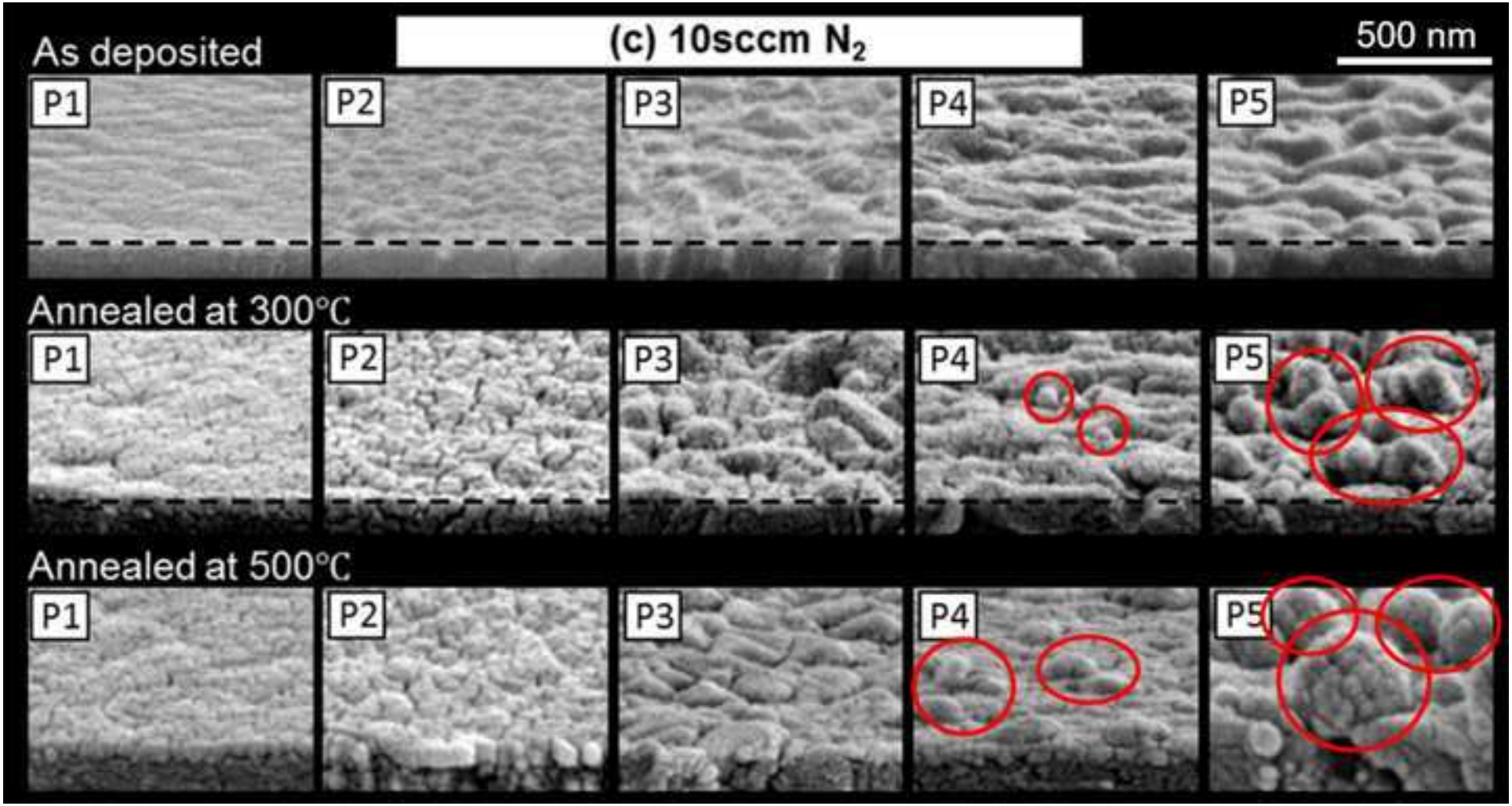

Figure 4

Click here to download high resolution image

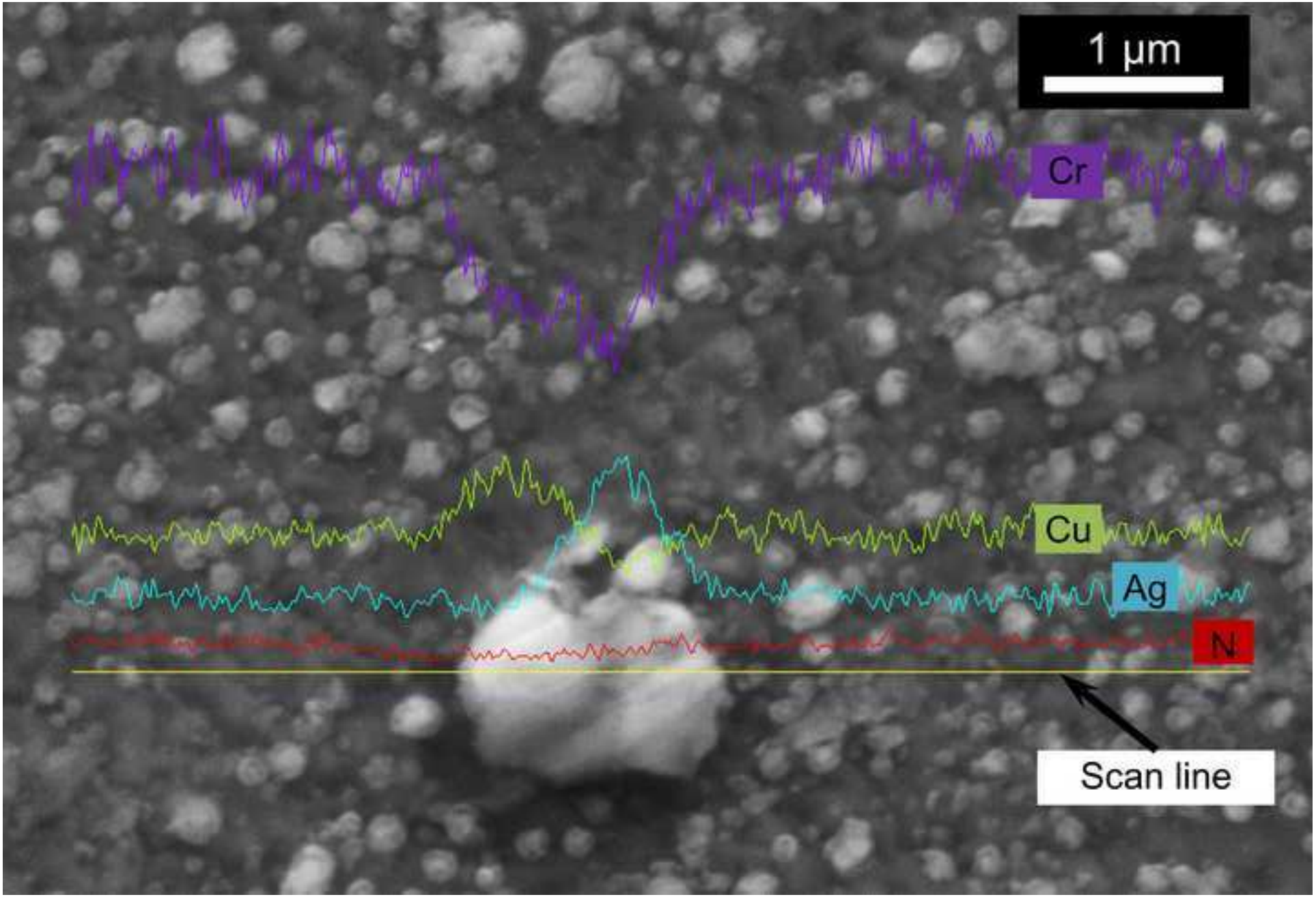

Figure 5

Click here to download high resolution image

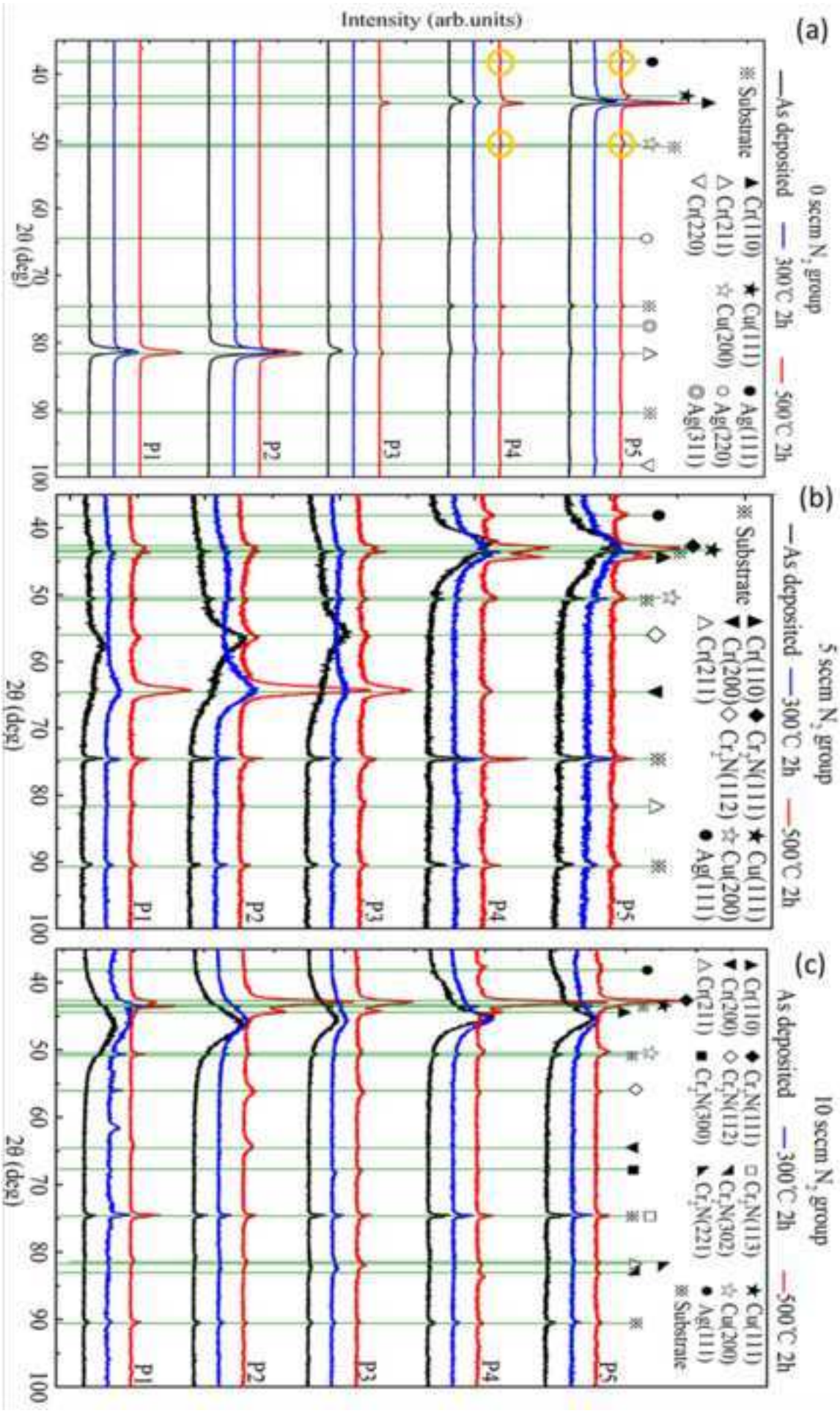

Figure 6

Click here to download high resolution image

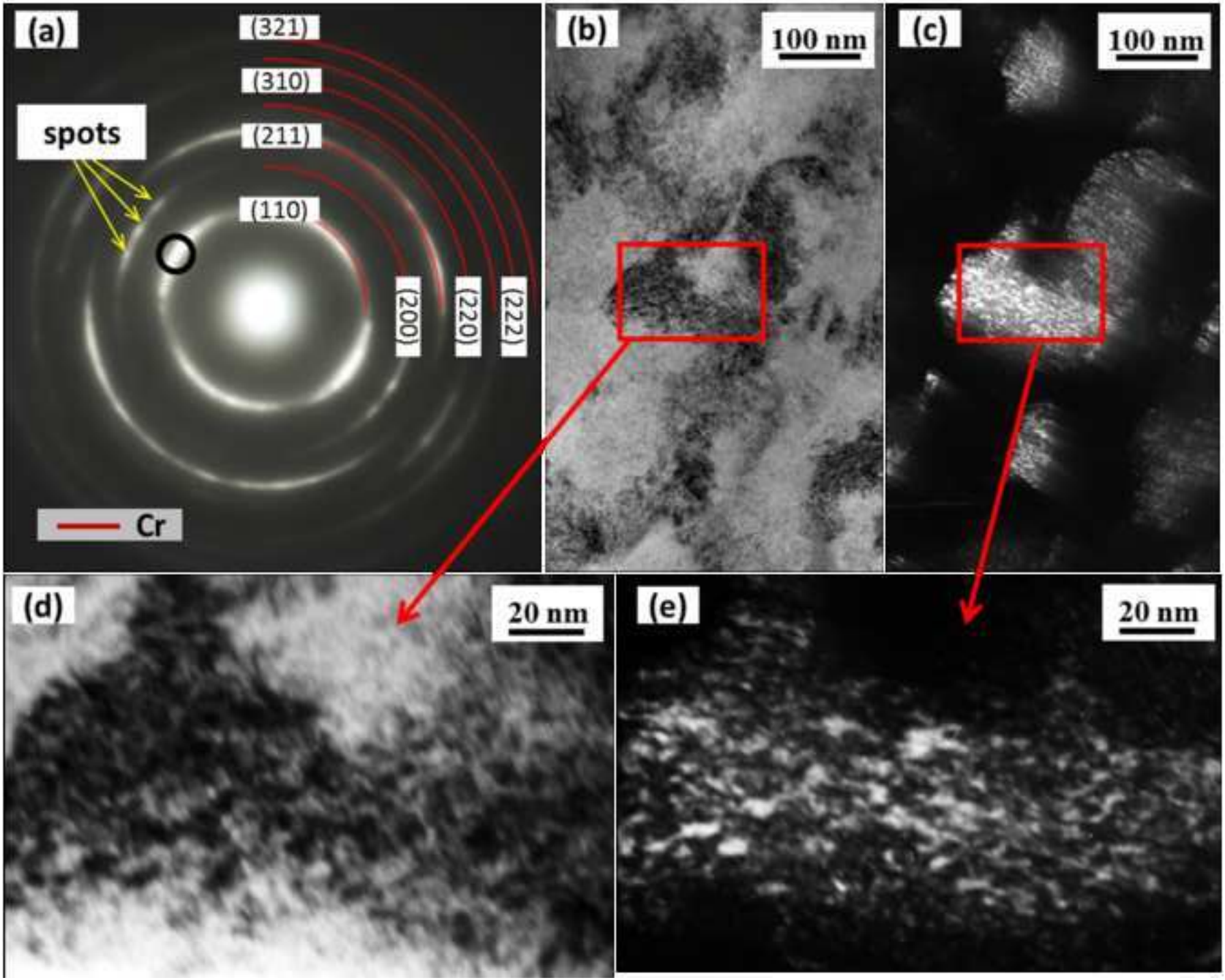

Figure 7

Click here to download high resolution image

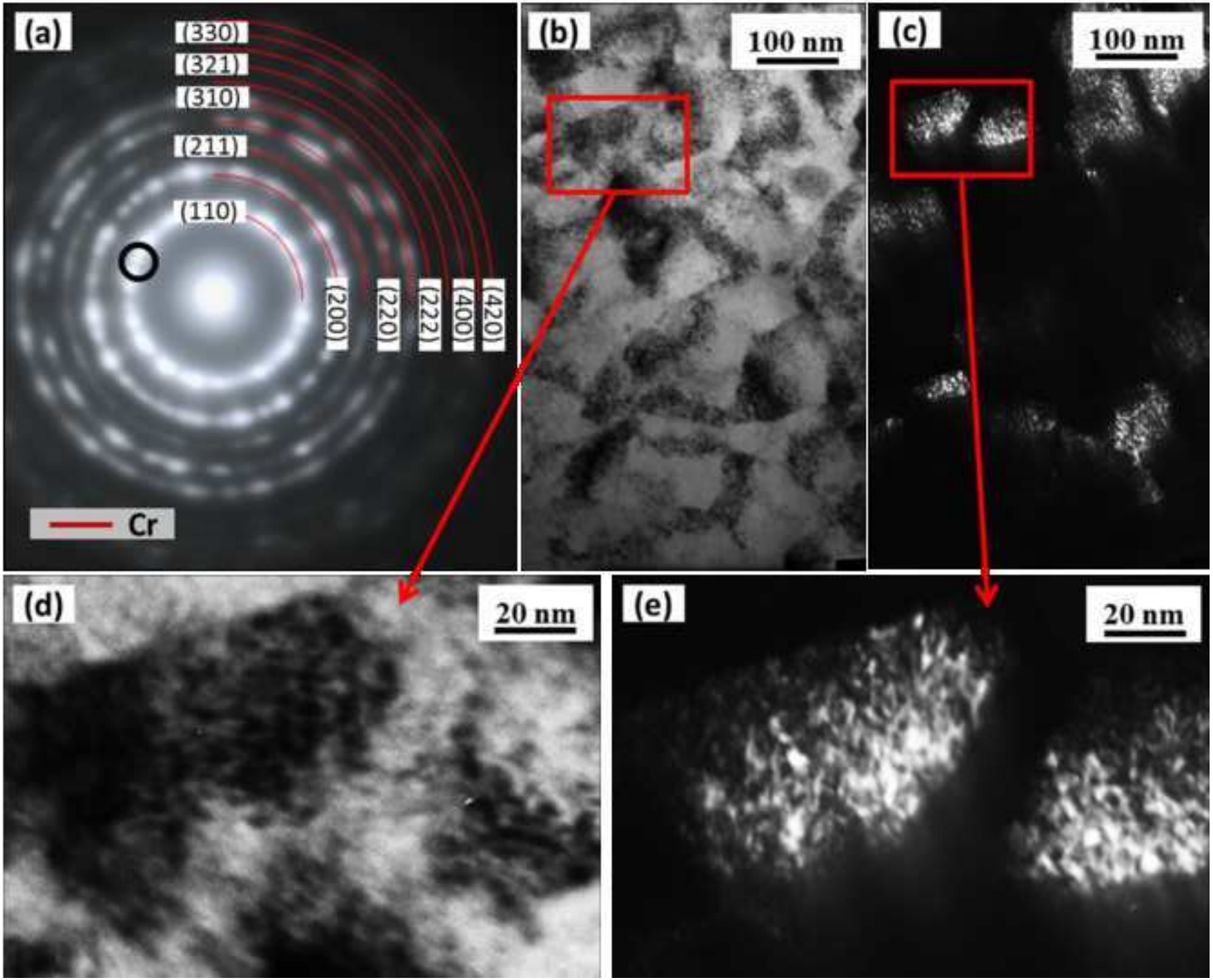

Figure 8

Click here to download high resolution image

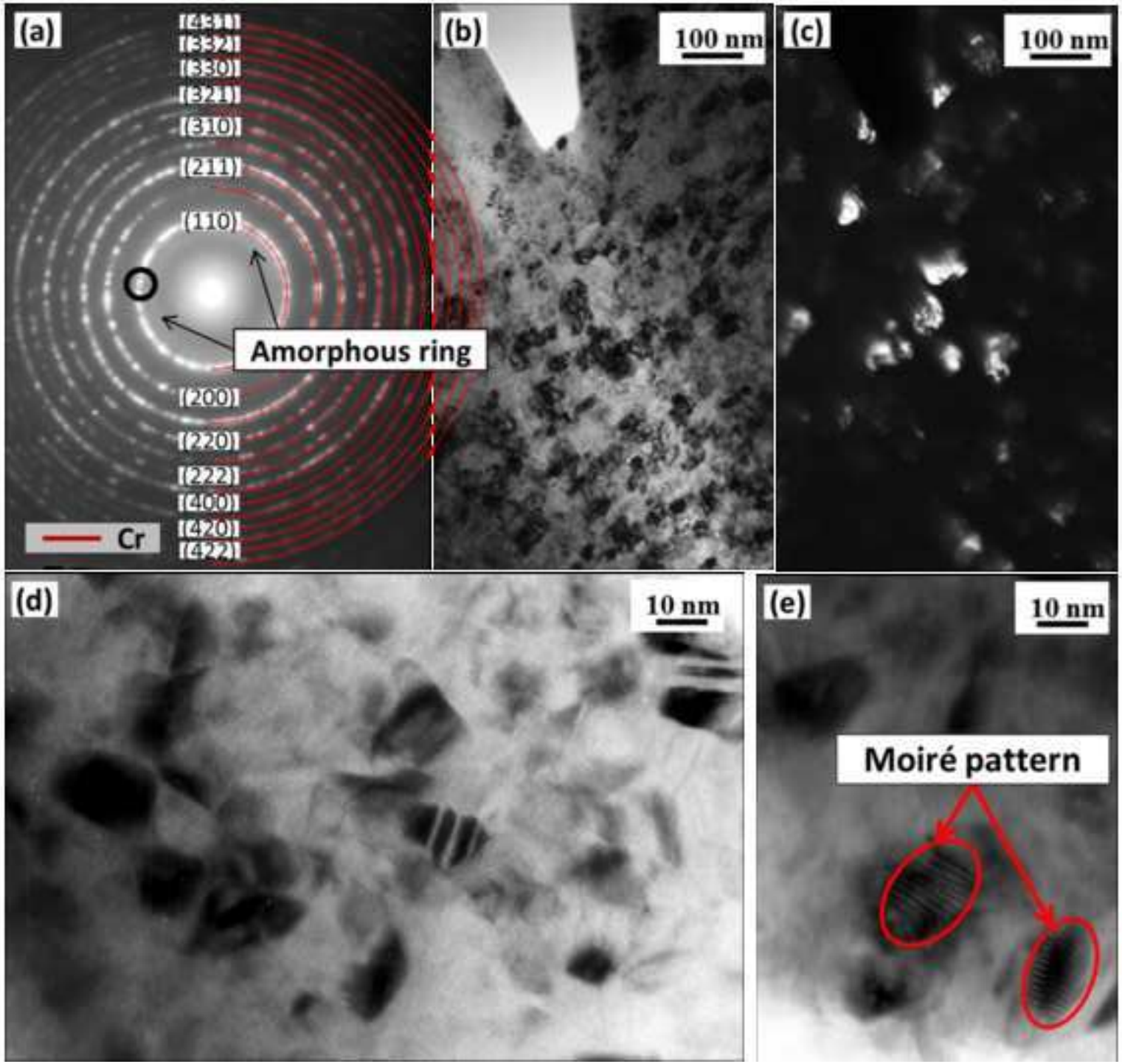

Figure 9

Click here to download high resolution image

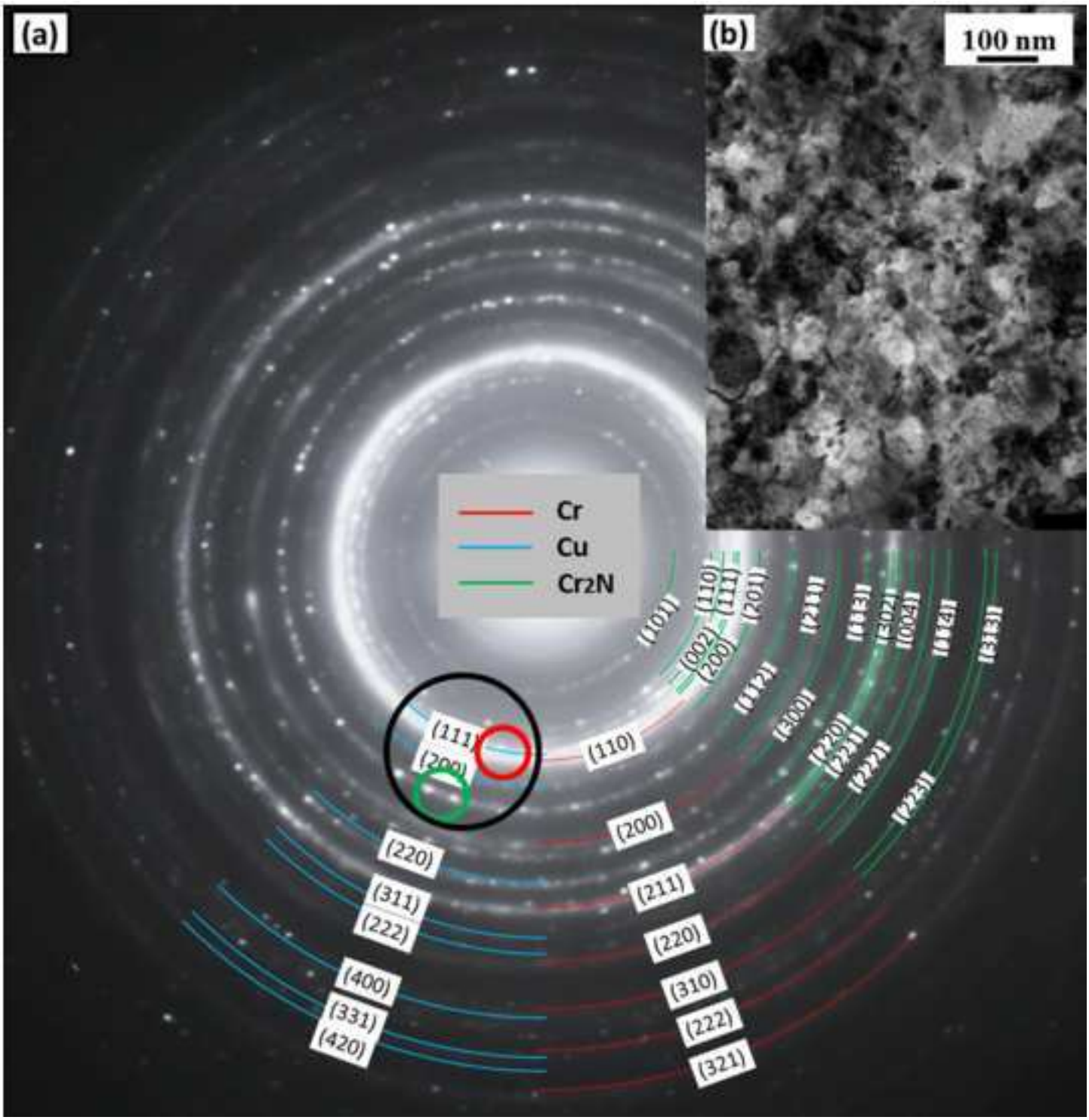

Figure 10
Click here to download high resolution image

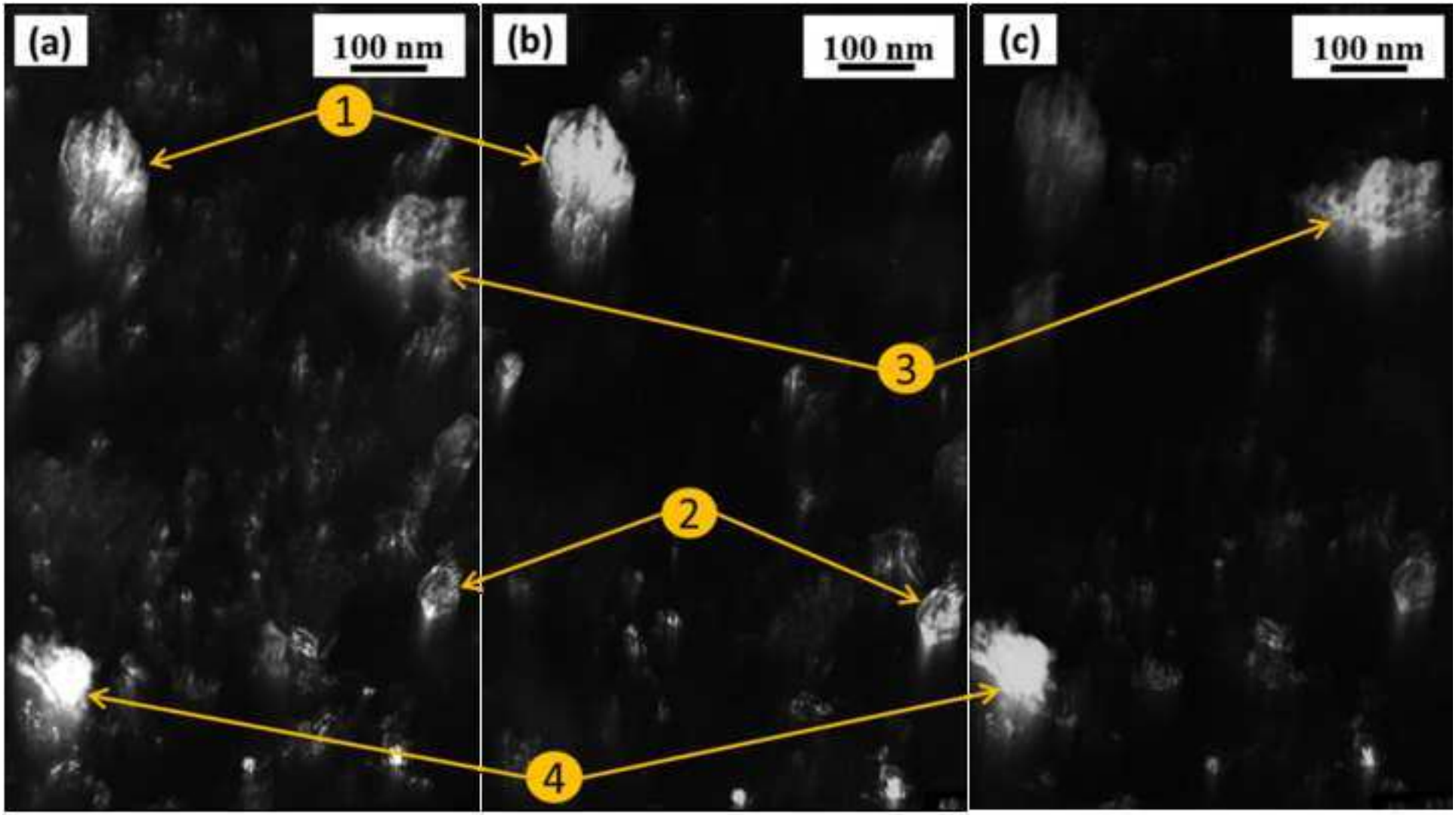

Figure 11

Click here to download high resolution image

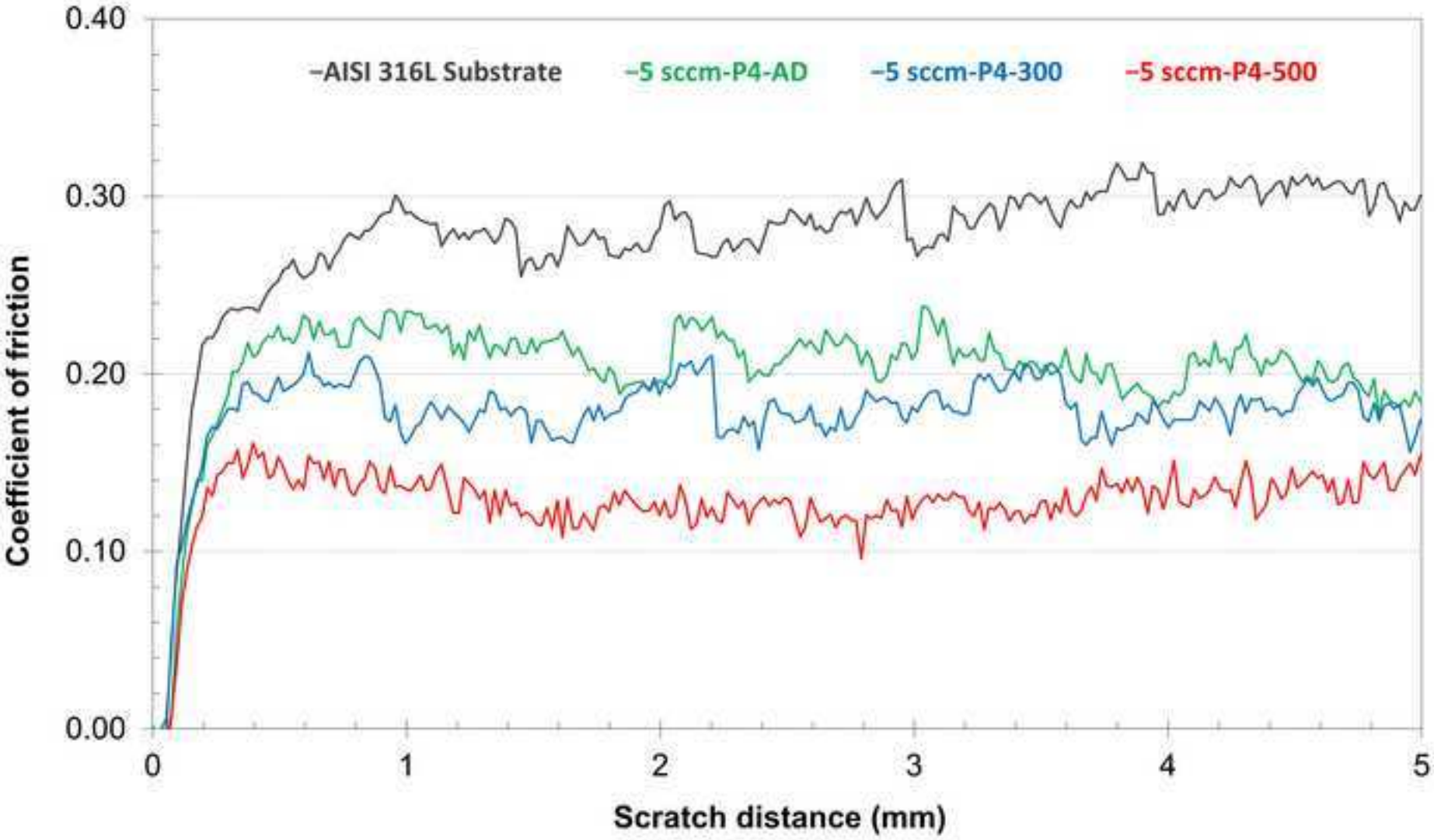

Figure 12

Click here to download high resolution image